Effects of an axisymmetric contraction on a turbulent pipe flow

Seong Jae Jang[1]**, Hyung Jin Sung**[1]†**and Per-Åge Krogstad**[2]

[1] Department of Mechanical Engineering, KAIST, 291 Daehak-ro, Yuseong-gu, Daejeon, 305-701, Korea

[2] Department of Energy and Process Engineering, Norwegian University of Science and Technology, N-7491, Trondheim, Norway

The flow in an axisymmetric contraction fitted to a fully developed pipe flow is experimentally and numerically studied. The reduction in turbulence intensity in the core region of the flow is discussed on the basis of the budgets for the various turbulent stresses as they develop downstream. The contraction generates a corresponding increase in energy in the near-wall region, where the sources for energy production are quite different and of opposite sign compared to the core region, where these effects are caused primarily by vortex stretching. The vortices in the pipe become aligned with the flow as the stretching develops through the contraction. Vortices which originally have a spanwise component in the pipe are stretched into pairs of counter-rotating vortices which become disconnected and aligned with the mean flow. The structures originating in the pipe which are inclined at an angle with respect to the wall are rotated towards the local mean streamlines. In the very near-wall region and the central part of the contraction the flow tends towards two-component turbulence, but these structures are different. The streamwise and azimuthal stresses are dominant in the near-wall region, while the lateral components dominate in the central part of the flow. The two regions are separated by a rather thin region where the flow is almost isotropic.

Key words: pipe flow boundary layer, shear layer turbulence, vortex interactions

1. Introduction

Flow subjected to strong axisymmetric strain in the streamwise direction has considerable engineering interest. The viscous flow near a stagnation point, such as for an impinging jet, experiences a strong deceleration which causes a rapid change in the turbulent structure. Equally frequent are the contracting flows found in pipes where a sudden area reduction is experienced, e.g. in the case where a large pipe is connected to a smaller one or when a metering orifice is inserted in the pipe. In the pipe systems of an alumina refinery plant, the scale deposition rate on the surface of an axisymmetric contraction increases 2- to 3-fold compared to that of adjacent straight pipes (Nawrath, Khan & Welsh 2006). Deposition of scale is undesirable, as it results in the reduction of the active diameter or even in a complete blockage of pipes.

† Email address for correspondence: hjsung@kaist.ac.kr

The direct cost of scale removal may contribute to as much as one quarter of the operational costs of an alumina refinery. Such deposition is significantly affected by the near-wall effects of a contraction. Metering nozzles with geometries regulated by international standards, which are used when trading with oil and natural gas between countries, for example, are perhaps among the economically most important examples. Errors of the order of fractions of one per cent in the estimated flow rates may imply millions of dollars of extra cost or income to the parties. It is therefore important to understand what happens to the turbulence when the flow is exposed to rapid straining.

The most studied case of the effect that a contracting flow has on the turbulence has been the reduction in turbulent energy in wind tunnels caused by a strong contraction. Based on a conservation of energy principle, Prandtl (1933) derived expressions for the amount of reduction in the streamwise turbulence intensity that could be obtained by a positive streamwise strain. This theory was improved by Taylor (1935), who studied the problem from a vortex stretching point of view. The problem of rapid distortions is treated in Fourier space by Batchelor (1953), assuming that the changes happen so quickly that turbulent inertia and viscous forces may be neglected. This leads to a predicted reduction in the streamwise normal stress by $(u_x'^2(\zeta))/(u_x'^2(\zeta = 1)) = (3/4\zeta^2)(\log(4\zeta^3) - 1)$ and a linear increase in the lateral components by $(u_r'^2(\zeta) + u_\theta'^2(\zeta))/(u_r'^2(\zeta = 1) + u_\theta'^2(\zeta = 1)) = (3/4)\zeta$ when the area contraction ratio ζ is large enough. In this case it was assumed that the initial turbulence was isotropic and the turbulence level was sufficiently low to allow the equations of motion to be linearized. While the predicted change in the streamwise normal stress is in good agreement with observations, the equations for the changes in the lateral components appear to significantly overpredict the increase in the turbulent lateral energy.

Since these early analytical treatments of the straining effect on homogeneous turbulence, a large number of analytical, numerical and experimental investigations have been undertaken. The flow has been studied in experiments so the effects on the mean flow and second-order moments are well known in the core region. Uberoi (1956) investigated the effects of contraction ratio and Reynolds number. He found that the longitudinal component decreases and the lateral component increases as the flow accelerates through the contraction in absolute magnitudes, and the turbulence Reynolds number has an insignificant effect on the performance of a nozzle. To improve the isotropy of grid generated turbulence for the Reynolds stress tensor, Uberoi & Wallis (1966) and Comte-Bellot & Corrsin (1966) used a contraction downstream of the grid with area ratios of 1.25 and 1.27, respectively. Both studies found that the turbulence was nearly isotropic at the exit of these contractions. However, the results of the studies are different in the way the flow developed further downstream. The results of Comte-Bellot & Corrsin (1966) indicate that the isotropy persisted downstream of the contraction, whereas the turbulence tended to return to its pre-contraction value in the results of Uberoi & Wallis (1966). Hussain & Ramjee (1976) investigated the effect of the contraction shape with the same contraction ratio. They found that the mean velocity and normal turbulence intensities in the core region at the exit plane are unaffected by the contraction shape. In most of the measurements performed along the symmetry axis of nozzles with a high contraction ratio, the streamwise turbulence intensity first decreases and then increases again downstream in the nozzle. Ertunç & Durst (2008) proposed measurement and correction methods to detect and eliminate all major contaminations of velocity fluctuation measurements. They found that, after applying the proposed correction

methods, the streamwise turbulence intensity does not show any sign of increase in the nozzle at high contraction ratios. The correction effect was also strong for the transverse turbulent stresses.

Improved prediction methods became available as the rapid distortion theory (RDT) was developed. Information about RDT may be found in Pope (2000), for example, and the review paper by Savill (1987) gives information about how the theory performs when the assumptions implicit in the method are not met. RDT may fail if the distortion is not sufficiently fast for the viscous terms to be neglected or if the turbulent energy level is not sufficiently low to allow the equations to be linearized. For the case investigated in the present paper, which consists of a contraction fitted at the end of a fully developed pipe flow, the centreline turbulence level is low but the contraction is too long for viscous effects to be negligible. Therefore one may expect RDT to predict an excessively fast distortion of the flow, as shown by Sreenivasan & Narasimha (1978).

The effects of the axisymmetric contraction are well known along the axis of symmetry of the contraction through previous studies. However, there seems to be much more uncertainty as to the effect of the contraction on the lateral components. In the present study, experiment and direct numerical simulation (DNS) are performed to elucidate the effects of an axisymmetric contraction on a turbulent pipe flow. With the introduction of DNS the flow structure in a contraction can be studied with high degree of accuracy and in much more detail than is available from RDT. The purpose of the present study has therefore been to perform DNS on a case where classical methods are expected to fail. Obviously the current setup produces strong anisotropy, due to the dominating cross-stream fluctuations. The streamwise vortex stretching increases the angular velocity, suppressing streamwise energy in favour of cross-stream fluctuations. The phenomenon is clearly connected to the influences of redistribution and secondary production terms, caused by the streamwise acceleration. To investigate the effects of Re, direct numerical simulations are presented for $Re = 5300$ and $15\,000$. The experiment was carried out at $Re = 35\,000$ for the same geometry. This was the lowest Re for which high-accuracy data could be obtained in the present test rig. Some Re effects must therefore be accounted for when comparing the DNS and the measured data. The contraction ratio in the experiment was $\zeta_o = 8$ and the test rig is shown in figure 1(*a*). The effects of the contraction ratio are also examined in the low-Re direct numerical simulations, which are performed for three contraction ratios, $\zeta_o = 2$, 4 and 8. The variations of the Reynolds stresses in the contraction are scrutinized and the budgets of the Reynolds stress equations are examined. Finally instantaneous flow fields and the conditional structures are analysed to characterize the response of the vortical structures in the contraction. In this paper we hope to shed more light on how the streamwise mean strain rate modifies the structure of the turbulence in the flow.

2. Experimental details

The experiment was undertaken in the fully developed pipe flow test rig at the Norwegian University of Science and Technology. The internal pipe diameter is $D = 186$ mm and the length of the pipe corresponds to 83 diameters. The pipe is fitted with pressure taps roughly at $8D$ intervals. At the entrance the pipe was fitted with honeycombs and screens. The flow underwent a natural transition, as no tripping of the flow was made. For a fully developed pipe flow the centreline turbulence intensity is of the order of $T_u = \sqrt{u_x'^2}/U \approx 3.5\,\%$, and since a considerable reduction through the contraction was anticipated, it is essential to keep other disturbances at a minimum.
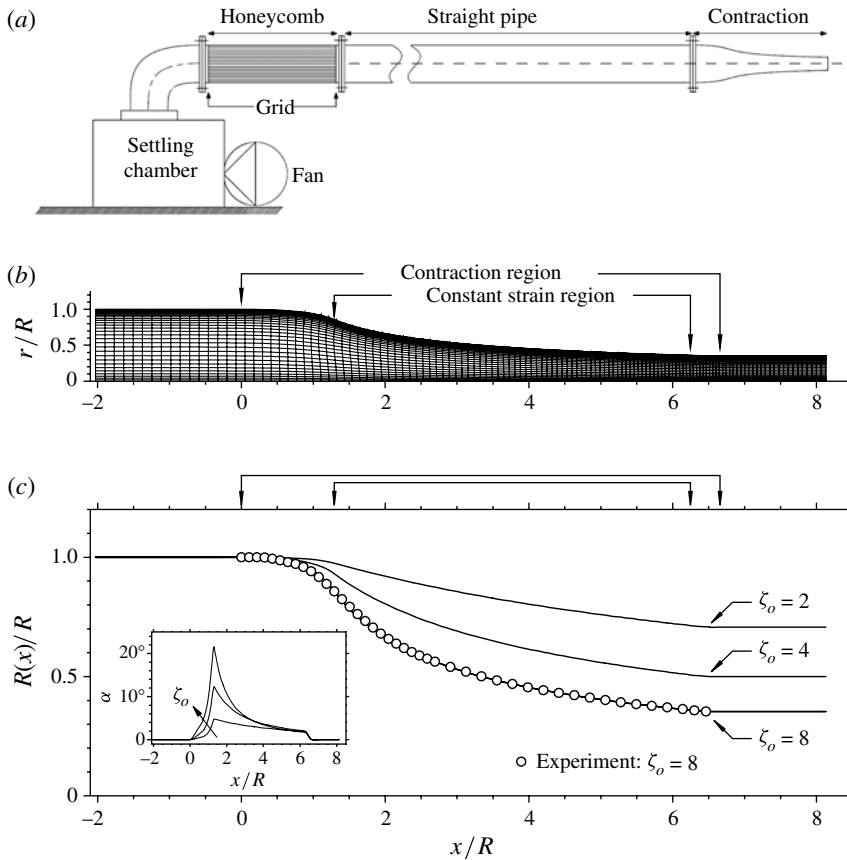
FIGURE 1. Contraction design. (*a*) Pipe rig facility; (*b*) computation domain in the *x*–*r* plane and grid points for $Re = 5300$ with $\zeta_o = 8$ (grid points are plotted only at every fourth point for clarity); (*c*) local contraction radius distribution. The inset shows the wall angle.

The test rig was therefore fitted with a large labyrinth settling chamber with damping material inside. This was mounted behind the fan and connected to the pipe by means of a flexible tube. In this way the pressure fluctuations generated by the fan were eliminated. At the outlet, the pipe was fitted with contractions of various area ratios. Here we concentrate on the one with the highest contraction ratio, $\zeta_o = 8$. The length of the contraction was 600 mm or about $3.2D$ and its shape was designed so that the area-averaged mean velocity increased linearly from about $x \sim 1D$ into the contraction. The design strain rate was $\mathrm{d}U_m(x)/\mathrm{d}x = 40 \ \mathrm{s}^{-1}$. The shape of the contraction is shown as circles in figure 1(*c*). The bulk velocity in the pipe for the present case was $U_{m,in} = 2.83 \ \mathrm{m \ s}^{-1}$, which produced a Reynolds number of $Re = U_{m,in}D/\nu \approx 35\,000$.

All data were taken using purpose-made single- and two-component hot-wire probes. All probes were fitted with partly etched Pl-10 %Rh Wollaston wires. The mean flow and second-order moments were obtained using 0.4 mm long 2.54 μm diameter wires. The two-component probes were all fitted with 0.5 mm long wires with 2.54 μm diameter. This corresponds to a spatial resolution of better than one Kolmogorov length along the centreline of the pipe for all probes, deteriorating slightly as the measurement points were shifted into the contraction. The probes were all calibrated *in situ* by moving them close to the centreline and traversing a miniature total

pressure probe equally far from the opposite side of the centreline. A fourth-order polynomial was used to fit the voltage-velocity characteristics of the probe and the effective angle method was used to describe the angular dependence of the signal when using two-component probes. Further details of the calibration procedures may be found in Bakken & Krogstad (2004). Purpose-made low-noise anemometers, filters and amplifiers were also made for this experiment. The amplifiers were adjusted to cover as much as possible of the range of the acquisition system and the filter cut-off frequency was continuously adjusted to the frequency where noise started to affect the dissipation spectrum. This ensures that the entire energy content in the signal is captured. The sampling frequency was then set according to the Nyquist criterion.

3. Numerical method

The governing equations are the continuity and the Navier–Stokes equations for an incompressible flow in cylindrical coordinates:

$$\frac{\partial u_x}{\partial x} + \frac{1}{r}\frac{\partial r u_r}{\partial r} + \frac{1}{r}\frac{\partial u_\theta}{\partial \theta} = 0, \tag{3.1}$$

$$\left.\begin{aligned}
&\frac{\partial u_x}{\partial t} + \frac{\partial(u_x u_x)}{\partial x} + \frac{\partial(u_r u_x)}{\partial r} + \frac{(u_r u_x)}{r} + \frac{1}{r}\frac{\partial(u_\theta u_x)}{\partial \theta} \\
&\quad = -\frac{1}{\rho}\frac{\partial p}{\partial x} + \nu\left\{\frac{\partial^2 u_x}{\partial x^2} + \frac{\partial^2 u_x}{\partial r^2} + \frac{1}{r}\frac{\partial u_x}{\partial r} + \frac{1}{r^2}\frac{\partial^2 u_x}{\partial \theta^2}\right\}, \\
&\frac{\partial u_r}{\partial t} + \frac{\partial(u_x u_r)}{\partial x} + \frac{\partial(u_r u_r)}{\partial r} + \frac{(u_r u_r - u_\theta u_\theta)}{r} + \frac{1}{r}\frac{\partial(u_\theta u_r)}{\partial \theta} \\
&\quad = -\frac{1}{\rho}\frac{\partial p}{\partial r} + \nu\left\{\frac{\partial^2 u_r}{\partial x^2} + \frac{\partial^2 u_r}{\partial r^2} + \frac{1}{r}\frac{\partial u_r}{\partial r} + \nu\frac{1}{r^2}\frac{\partial^2 u_r}{\partial \theta^2} - \frac{2}{r^2}\frac{\partial u_\theta}{\partial \theta} - \frac{u_r}{r^2}\right\}, \\
&\frac{\partial u_\theta}{\partial t} + \frac{\partial(u_x u_\theta)}{\partial x} + \frac{\partial(u_r u_\theta)}{\partial r} + 2\frac{(u_r u_\theta)}{r} + \frac{1}{r}\frac{\partial(u_\theta u_\theta)}{\partial \theta} \\
&\quad = -\frac{1}{\rho}\frac{1}{r}\frac{\partial p}{\partial \theta} + \nu\left\{\frac{\partial^2 u_\theta}{\partial x^2} + \frac{\partial^2 u_\theta}{\partial r^2} + \frac{1}{r}\frac{\partial u_\theta}{\partial r} + \frac{1}{r^2}\frac{\partial^2 u_\theta}{\partial \theta^2} + \frac{2}{r^2}\frac{\partial u_r}{\partial \theta} - \frac{u_\theta}{r^2}\right\}.
\end{aligned}\right\} \tag{3.2}$$

The bulk velocity $U_{m,in}$ and the radius R at the inlet are used for non-dimensionalization. The Reynolds number is defined as $Re = U_{m,in}D/\nu$, where D is the diameter of the inlet. To simulate the flow in the axisymmetric contraction, we introduce the generalized coordinates for the streamwise and radial directions, i.e. $(x, r) \rightarrow (\eta^1, \eta^2)$, and use a cylindrical coordinate for azimuthal direction ($\theta = \eta^3$). The velocity components are transformed into the volume fluxes across the faces of the cells q^i or $\boldsymbol{q}$, which are equivalent to using the contravariant velocity components on a staggered grid multiplied by the Jacobian of the coordinate transformation. The transformed governing equations can be written as

$$\frac{1}{r}\frac{1}{J}\frac{\partial r q^1}{\partial \eta^1} + \frac{1}{r}\frac{1}{J}\frac{\partial r q^2}{\partial \eta^2} + \frac{1}{r}\frac{\partial q^3}{\partial \eta^3} = 0, \tag{3.3}$$

$$\frac{\partial q^i}{\partial t} + N^i(\boldsymbol{q}) = -G^i(p) + L_1^i(\boldsymbol{q}) + L_2^i(\boldsymbol{q}), \tag{3.4}$$

where N^i is the convective term, $G^i(p)$ is the pressure gradient term, L_1^i and L_2^i are the diffusion terms without and with cross-derivatives, respectively. The terms in (3.4) are,

for $i = 1, 2$,

$$
\left.
\begin{aligned}
N^i &= \frac{1}{r}\frac{1}{J}\gamma_m^i\frac{\partial}{\partial\eta^j}\frac{1}{J}rc_k^m q^k q^j; \quad i = k \\
&+ \frac{1}{J}\gamma_m^i\frac{\partial}{\partial\eta^j}\frac{1}{J}c_k^m q^k q^j; \quad i \neq k \\
&+ \frac{1}{r}\frac{\partial}{\partial\eta^3}q^i q^3 - \frac{1}{r}\gamma_2^i q^3 q^3, \\
G^i(p) &= \frac{1}{\rho}\alpha^{ij}\frac{\partial p}{\partial\eta^j}, \\
L_1^i &= \nu\frac{1}{r}\frac{1}{J}\gamma_m^i\frac{\partial}{\partial\eta^k}r\alpha^{kj}\frac{\partial}{\partial\eta^j}\frac{1}{J}c_l^m q^l + \nu\frac{1}{r^2}\frac{\partial}{\partial\eta^3}\frac{\partial}{\partial\eta^3}q^i; \quad j = k \\
&- \nu\frac{1}{r^2}\gamma_2^i\frac{1}{J}c_l^2 q^l - \nu\frac{2}{r^2}\gamma_2^i\frac{\partial}{\partial\eta^3}q^3, \\
L_2^i &= \nu\frac{1}{r}\frac{1}{J}\gamma_m^i\frac{\partial}{\partial\eta^k}r\alpha^{kj}\frac{\partial}{\partial\eta^j}\frac{1}{J}c_l^m q^l; \quad j \neq k,
\end{aligned}
\right\}
\tag{3.5}
$$

for $i = 3$,

$$
\left.
\begin{aligned}
N^3 &= \frac{1}{r}\frac{1}{J}\frac{\partial}{\partial\eta^j}rq^j q^3 + \frac{1}{r}\frac{\partial}{\partial\eta^3}q^3 q^3 + \frac{1}{r}\frac{1}{J}c_j^2 q^j q^3, \\
G^3(p) &= \frac{1}{\rho}\frac{1}{r}\frac{\partial p}{\partial\eta^3}, \\
L_1^3 &= \nu\frac{1}{r}\frac{1}{J}\frac{\partial}{\partial\eta^k}r\alpha^{kj}\frac{\partial}{\partial\eta^j}q^3 + \nu\frac{1}{r^2}\frac{\partial}{\partial\eta^3}\frac{\partial}{\partial\eta^3}q^3; \quad j = k \\
&- \nu\frac{1}{r^2}q^3 + \nu\frac{2}{r^2}\frac{\partial}{\partial\eta^3}\frac{1}{J}c_j^2 q^j, \\
L_2^3 &= \nu\frac{1}{r}\frac{1}{J}\frac{\partial}{\partial\eta^k}r\alpha^{kj}\frac{\partial}{\partial\eta^j}q^3; \quad j \neq k,
\end{aligned}
\right\}
\tag{3.6}
$$

where $q^j = \gamma_k^j u_k$, $q^3 = u_3$, $c_k^j = \partial x_j/\partial\eta^k$, $\gamma_k^j = J(c_j^k)^{-1}$, $\alpha^{jk} = J(c_j^m c_k^m)^{-1}$, $J = (\|c_j^m c_k^m\|)^{\frac{1}{2}}$, $(x_1, x_2, x_3) = (x, r, \theta)$, $(u_1, u_2, u_3) = (u_x, u_r, u_\theta)$ and $j, k, l, m = 1, 2$. These terms are similar to those proposed by Choi, Moin & Kim (1993), who introduced generalized coordinates based on Cartesian coordinates.

The governing equations are integrated in time by using the fully implicit fractional step method. All terms are advanced with the Crank–Nicolson method in time, and they are resolved using a second-order central difference scheme in space with a staggered grid. In the present study, we have tested two time-advanced methods: the fully implicit decoupling method proposed by Kim, Baek & Sung (2002) and the Newton iterative method (Choi *et al.* 1993). For the decoupling method, to ensure the numerical stability for rather large Courant–Friedrichs–Lewy (CFL) number ($CFL_{max} \sim 24$) for the azimuthal velocity component at the first radial grid, one additional iteration is needed for solving the intermediate velocity components whereas the velocity components are solved without iteration in the original method proposed by Kim *et al.* (2002). However, for the Newton iterative method, more than twelve iterations are needed to solve the discretized nonlinear momentum equations. As shown in figure 2, the results from the two methods are exactly the same, but the Newton iterative method requires about three-fold total CPU time. In the present study, computational cost can be reduced by using the fully implicit decoupling method.
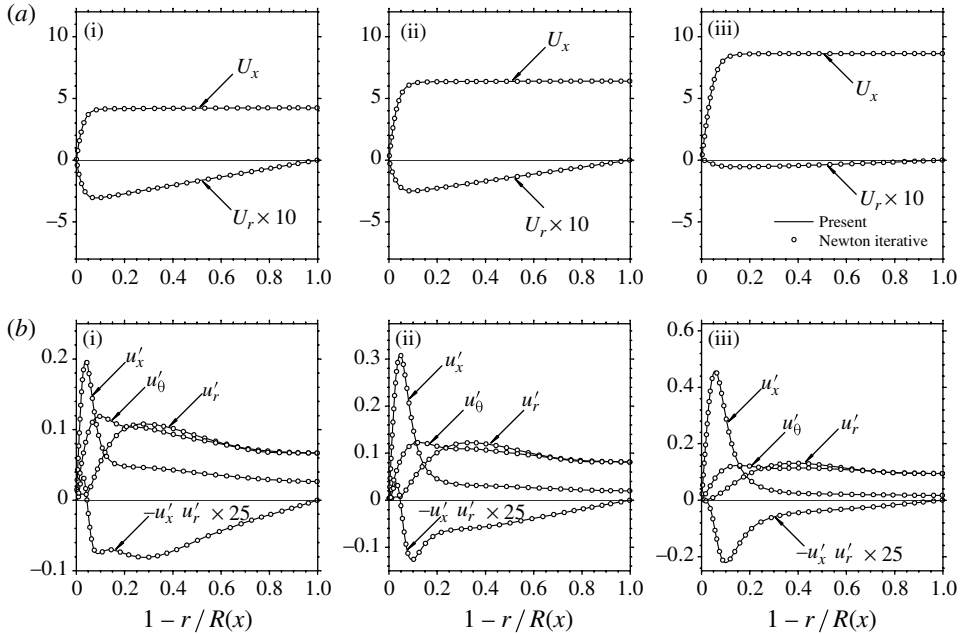
FIGURE 2. Comparison of the two methods: decoupling method (solid line) and Newton iterative method (circles), at $Re = 5300$ with $\zeta_o = 8$. (*a*) Mean velocity profile; (*b*) Reynolds stresses. (i) $x/R = 3.34$; (ii) $x/R = 4.90$; (iii) $x/R = 6.66$.

The transformed Poisson equation for p was solved via fast Fourier transform along the azimuthal direction and a multigrid algorithm was employed to accelerate the convergence of the iterative procedure.

Direct numerical simulations of a contraction turbulent pipe for two Reynolds numbers ($Re_{D,in} = 5300$ and $15\,000$) and three contraction ratios ($\zeta_o = 2$, 4 and 8) defined as the ratio of the inlet area to the outlet area are performed. The computational domain size is $L_x = 10.2R$, $L_r \leqslant R$ and $L_\theta = 2\pi$. The spatial and time resolutions are summarized in table 1, where $\Delta s_{\eta 1}^+$ is defined as the distance between two grid points at the solid wall and $\Delta s_{\eta 2}^+$ is the distance of the grid point in the immediate vicinity of the wall. Non-uniform grid distributions were used in the streamwise and radial directions, whereas a uniform grid distribution was used in the azimuthal direction. To obtain the grid orthogonality at the boundary and the grid clustering in the interior of the computational domain, an elliptic grid generation method proposed by Spekreijse (1995) was used based on a composite mapping of a nonlinear algebraic transformation and an elliptic transformation, shown in figure 1(*b*). The computational time step used is $\Delta t = 0.001R/U_{m,in}$ and $0.0005R/U_{m,in}$ for the cases of $Re = 5300$ and $15\,000$, respectively. The total averaging time to obtain the statistics is $132R/U_{m,in}$, sufficient to allow a particle to travel 17, 22 and 27 times through the whole axial dimension at the bulk velocity for the cases of $\zeta_o = 2$, 4 and 8, respectively. Statistical quantities are averaged over time and the azimuthal direction.

Auxiliary simulations of the fully developed turbulent pipe flow were carried out separately to obtain the inflow data. The stored instantaneous plane data of velocities in the inflow simulation are provided at the inlet of the main simulation for each time step. The convective outflow condition $\partial u/\partial t + c\partial u/\partial x = 0$ is applied at the outlet

$Re_{D,in}$	$Re_{D,out}$	ζ_o	(N_x, N_r, N_θ)	$\Delta s_{\eta 1,min}^+$	$\Delta s_{\eta 1,max}^+$	$\Delta s_{\eta 2,min}^+$	$(R(x)\Delta\theta)_{max}^+$	Δt_{max}^+
5300	7510	2	(512,128,256)	4.22	7.32	0.13	7.12	0.07
5300	10 600	4	(512,128,256)	5.45	11.50	0.13	9.20	0.21
5300	14 990	8	(512,128,256)	5.32	18.60	0.13	11.20	0.62
15 000	42 430	8	(1280,192,640)	5.19	16.10	0.18	9.720	0.51

TABLE 1. Simulation details.
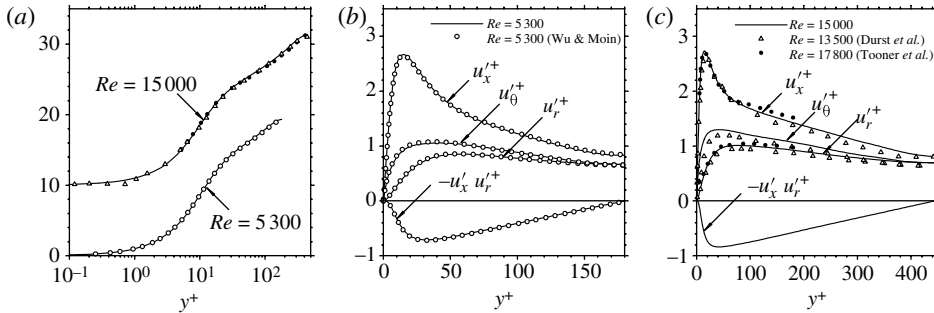
FIGURE 3. Comparison of turbulence statistics. (*a*) Mean velocity profile; (*b*) Reynolds stresses at $Re_{D,in} = 5300$; (*c*) Reynolds stresses at $Re_{D,in} = 15\,000$.

where c is the local bulk velocity. The no-slip condition is imposed at the solid wall. The centreline condition for the radial velocity is obtained by averaging corresponding values across the centreline (Akselvoll & Moin 1995). Derivatives of quantities that are staggered with respect to the centreline can be obtained by differencing opposing values across the centreline, accounting for reversals in the directions of the radial and azimuthal unit vectors through the centreline. The periodic condition is applied in the azimuthal direction. To ascertain the reliability and accuracy of the present numerical simulation, comparisons of the turbulence statistics with previously published data are made and presented in figure 3. The mean velocity profile normalized by the friction velocity is shown in figure 3(*a*), where $y^+ = (R - r)u_\tau/\nu$ and $U_x^+ = U_x/u_\tau$. Comparisons of the turbulence intensities and Reynolds shear stress are presented in figures 3(*b*) and 3(*c*). The present results are in good agreement with the previous data at both Reynolds numbers. This suggests that the resolution of the present study is sufficient to analyse the second-order turbulence statistics.

4. Results and discussion

4.1. *Mean properties*

First, we examine the variation of mean variables due to the axisymmetric contraction. Figure 4 shows the streamwise distributions of the bulk mean velocity and the mean strain based on $U_{m,in}$. The bulk mean velocity increases linearly in the constant strain region, where the normalized strain rates are $dU_m(x)/dx = 0.18$, 0.55 and 1.29 for systems with $\zeta_o = 2$, 4 and 8, respectively. The distributions of the pressure coefficient along the centreline, $C_p = (P_{c.l.}(x) - P_{c.l.,in})/(\rho U_{m,in}^2/2)$ are shown in figure 4(*c*). In all of the flows, C_p decreases monotonically all the way to the end of the computational domain. The streamwise pressure gradient decreases linearly in the constant strain
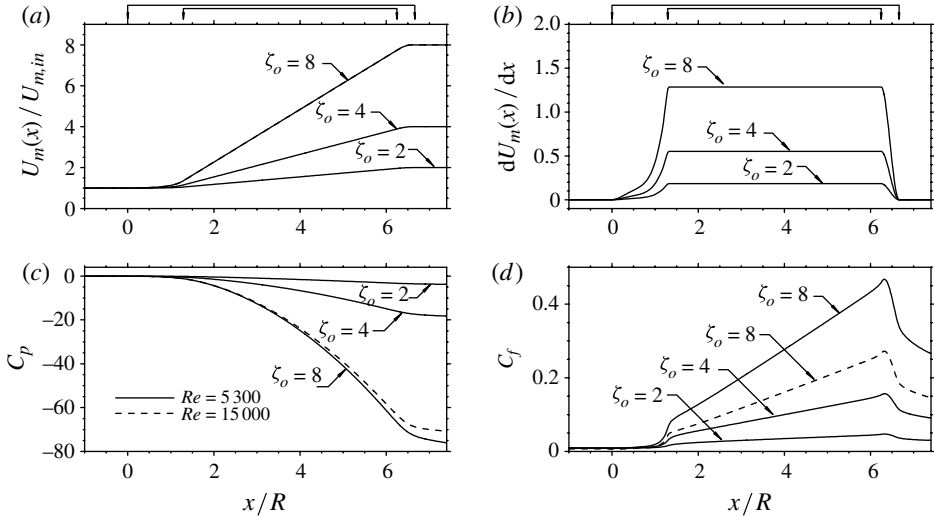
FIGURE 4. Streamwise distribution of (*a*) bulk velocity, (*b*) strain, (*c*) pressure coefficient at the centreline and (*d*) skin friction coefficient.
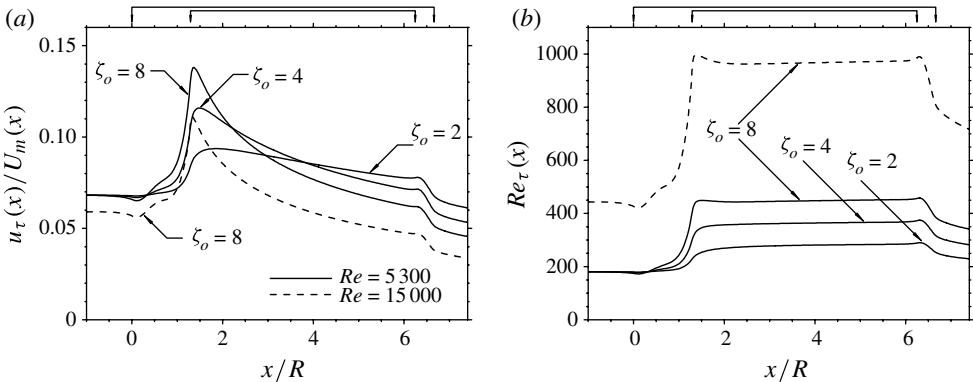

FIGURE 5. Streamwise distribution of (*a*) local friction velocity and (*b*) Re_τ.

region and becomes a minimum at the end of the constant strain region. Figure 4(*d*) shows the distributions of the skin friction coefficient, $C_f = \tau_w/(\rho U_{m,in}^2/2)$. In all of the flows, C_f increases linearly in the constant strain region $\tau_w \sim R(x)^{-2}$ in absolute magnitude. After this region where the strain decreases, C_f rapidly decreases. However, relative to C_f at the inlet, C_f is always higher when the flow enters the contraction. A slight Re-dependence is evident in the C_p distribution for two different Reynolds numbers with $\zeta_o = 8$ in figure 4(*c*). This comes from the significant differences in C_f. Figure 5 shows the variation of the friction velocity normalized with the local bulk velocity $U_m(x)$ and Re_τ defined as $Re_\tau(x) = u_\tau(x)R(x)/\nu$. The local friction velocity and Re_τ increase rapidly in the region where the wall angle, defined as the angle between the solid wall and the contraction axis, increases rapidly (figure 1*c*). In the constant strain region, the local friction velocity decreases monotonically and Re_τ becomes constant due to the relation of $\tau_w \sim R(x)^{-2}$.
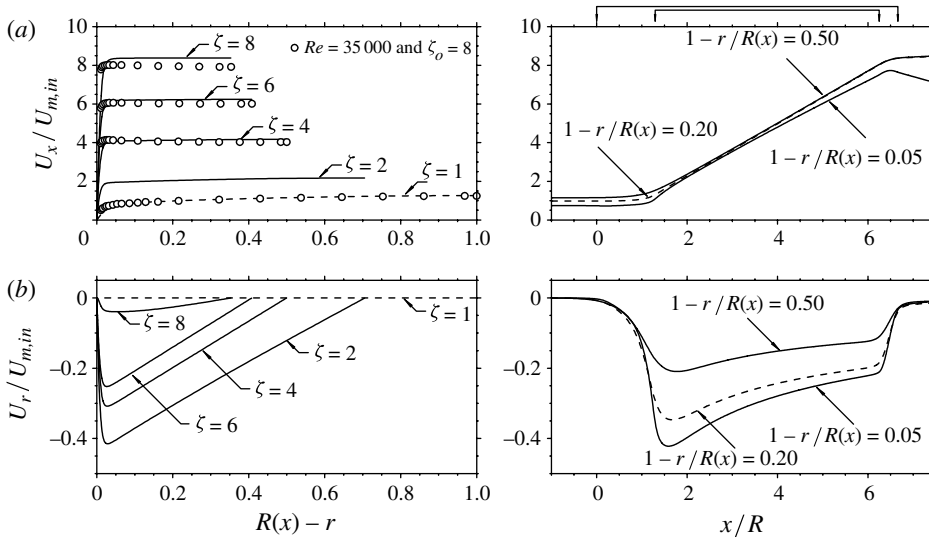
FIGURE 6. (*a*) Streamwise mean velocity and (*b*) radial mean velocity in the radial and streamwise direction for $Re = 15\,000$ with $\zeta_o = 8$. The locations of x/R are 1.79, 3.34, 4.90 and 6.66 for $\zeta = 2, 4, 6$ and 8, respectively.

Figure 6 shows the variation of mean velocities along the radial and streamwise directions for $Re = 15\,000$ with $\zeta_o = 8$. Due to the homogeneity in the azimuthal direction, the mean velocity vector reduces to $\boldsymbol{U} = [U_x(x, r), U_r(x, r), 0]$. The mean streamwise velocity increases and becomes very uniform as the local contraction ratio ($\zeta = U_m(x)/U_{m,in}$) increases, except for a very thin layer at the wall (figure 6a). The magnitude of $\mathrm{d}U_x/\mathrm{d}r$ increases in the inner region and drops to zero at the centreline. After $x/R = 2(\zeta = 2.3)$, the streamwise distributions of U_x are independent of r except very close to the wall and increase linearly, $\mathrm{d}U_x/\mathrm{d}x = \text{constant}$, in the range $1 - r/R(x) > 0.1$. Due to the contraction, negative radial velocity is generated from the wall to the centreline. U_r becomes a minimum very near the wall and then increases linearly to the centreline. This linear relation is easily obtained from the continuity equation for mean velocity when $\mathrm{d}U_x/\mathrm{d}x$ is constant, $\mathrm{d}U_r/\mathrm{d}r = -0.5\,\mathrm{d}U_x/\mathrm{d}x = \text{constant}$. For the streamwise direction, U_r decreases rapidly in the initial region of the contraction and gradually increases in the constant strain region until it increases rapidly when the streamwise acceleration ceases at the end region of the contraction. The variation trend of U_r magnitude is similar to that of the wall angle (figure 6b). Downstream of the contraction, a small negative U_r still remains. This means that U_x is decelerated in the inner region and accelerated in the outer region as the flow again develops towards a new state of fully developed pipe flow. The wall similarity is summarized in the Appendix.

4.2. *Second-order turbulence statistics*

The presence of an axisymmetric contraction significantly affects the turbulent flow statistics. Figure 7 shows the variation of turbulence intensities normalized by $U_{m,in}$ as a function of the radial distance from the wall, scaled with the local radius $R(x)$. Also included in the figures are the measurements for $\zeta_o = 8$ taken at $Re = 35\,000$. The streamwise component of the turbulence intensities is most significantly affected by the contraction in the outer region. For $\zeta_o = 2$, the streamwise component decreases in
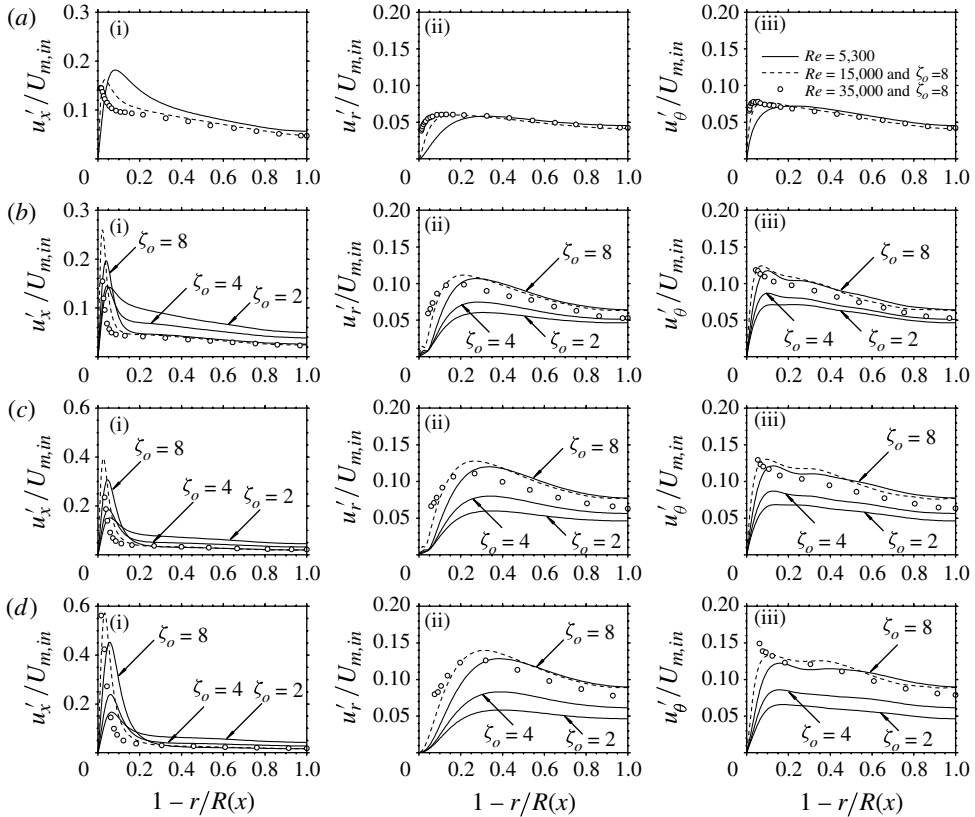
FIGURE 7. Turbulence intensities based on $U_{m,in}$. (*a*) Straight pipe; (*b*) $x/R = 3.34$; (*c*) $x/R = 4.90$; (*d*) $x/R = 6.66$. (i) Streamwise component; (ii) radial component; (iii) azimuthal component.

the outer region, whereas the radial and azimuthal components are similar to those of the straight pipe. For $\zeta_o = 4$ and 8, the radial variation of the streamwise component has two different regions in the contraction. As the local contraction ratio increases, the streamwise component increases in the inner region and decreases in the outer region. The near-wall peak locations in the streamwise component for $\zeta_o = 8$ are shifted closer to the wall and the peak value increases as *Re* increases. The global features of the radial and azimuthal components affected by the contraction are similar. The radial and azimuthal components relative to those of the straight pipe always increase in the contraction region except the radial component near the wall region $\sim 1 - r/R(x) = 0.05$, where the local minimum exists. This local minimum will be discussed later by the change of the coordinate system. When the contraction ratio is large enough ($\zeta_o = 4$ and 8), the radial and azimuthal components rapidly become dominant in the outer region. The turbulence intensities for $\zeta_o = 8$ are almost the same despite the different Reynolds numbers in the outer region. Thus, the contraction ratio is the main parameter for characterizing the second-order turbulence statistics in the outer region.

From previous experimental works of Uberoi (1956) and Ertunç & Durst (2008), it is well known that the streamwise component of the turbulent kinetic energy is reduced, but the lateral components are increased along the centreline. Figure 8 shows
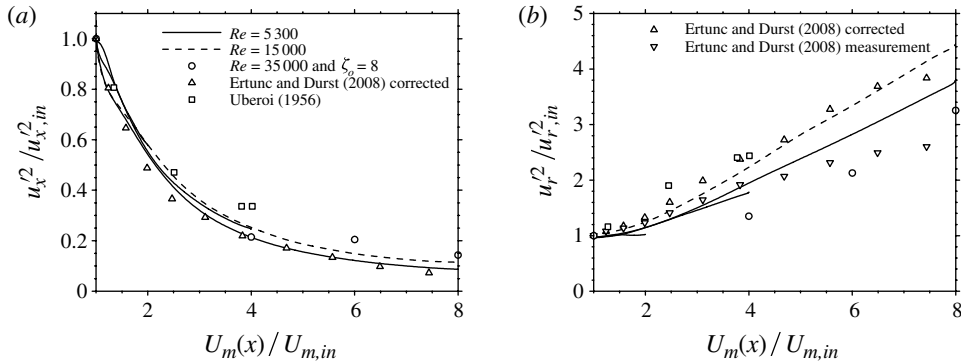
FIGURE 8. (*a*) Relative streamwise turbulent stress and (*b*) relative radial turbulent stress based on $U_{m,in}$, along the centreline.

the computed variations in the streamwise and radial turbulent stresses along the centreline, compared with the previous experiments. The data are normalized by the corresponding values from the straight pipe for comparison. The streamwise turbulent stress rapidly decreases where the bulk velocity is relatively low, whereas the radial turbulent stress increases almost linearly as the bulk velocity increases. The azimuthal component is identical to the radial component at the centreline and has therefore not been shown. The global trend of the variation of the turbulent stresses is in good agreement with the previous experimental data despite the differences in the geometry, *Re* and the contraction ratio. The data of Uberoi (1956) were measured from the contraction duct for $Re_m = 3710$ with $\zeta_o = 4$, and the data of Ertunç & Durst (2008) from the axisymmetric contraction for $Re_\lambda = 26.7$ with $\zeta_o = 14.75$. Ertunç & Durst (2008) showed that the error correction of the hot-wire measurement data is important when the contraction ratio is high, and the remarkable correction to the radial turbulent stress should be done for most of the experiments performed, especially with high contraction ratio nozzles.

Figure 9 shows the total turbulent kinetic energy $k = 0.5(u_x'^2 + u_r'^2 + u_\theta'^2)$ normalized by $U_{m,in}$. In the inner region, the rapid increase of k corresponds to that of the streamwise turbulence intensity. For $\zeta_o = 2$ and 4, k is unaffected by the contraction in the outer region. This means that the energy gain of the radial and azimuthal stresses is similar to the energy loss of the streamwise stress in the outer region. For $\zeta_o = 8$, the equilibrium of the energy redistribution between the streamwise and lateral stresses holds for $x/R < 3.34$. After this range, k gradually increases in the outer region. This increase indicates that the energy gain of the lateral stresses is more than the energy loss of the streamwise stress. The turbulence intensity based on the local bulk velocity is the major parameter in the design of the contraction. As the flow is accelerated, the streamwise turbulent stress vanishes in the outer region, thus the reliable turbulence intensity should be calculated from the total kinetic energy. The variation of the local turbulence intensity, defined as $T_k = \{(u_x'^2 + u_r'^2 + u_\theta'^2)/3\}^{1/2}$, is shown in figure 10. As the flow goes downstream, the local turbulence intensity first drops rapidly before $x/R = 3.34$ and then gradually decreases to the end of the contraction.

The energy partition parameter $K^* = 2u_x'^2/(u_r'^2 + u_\theta'^2)$ is calculated to see the relative contributions to the turbulent kinetic energy of the streamwise turbulent stress and the lateral turbulent stresses. In all of the flows, the peak location of K^* is slightly
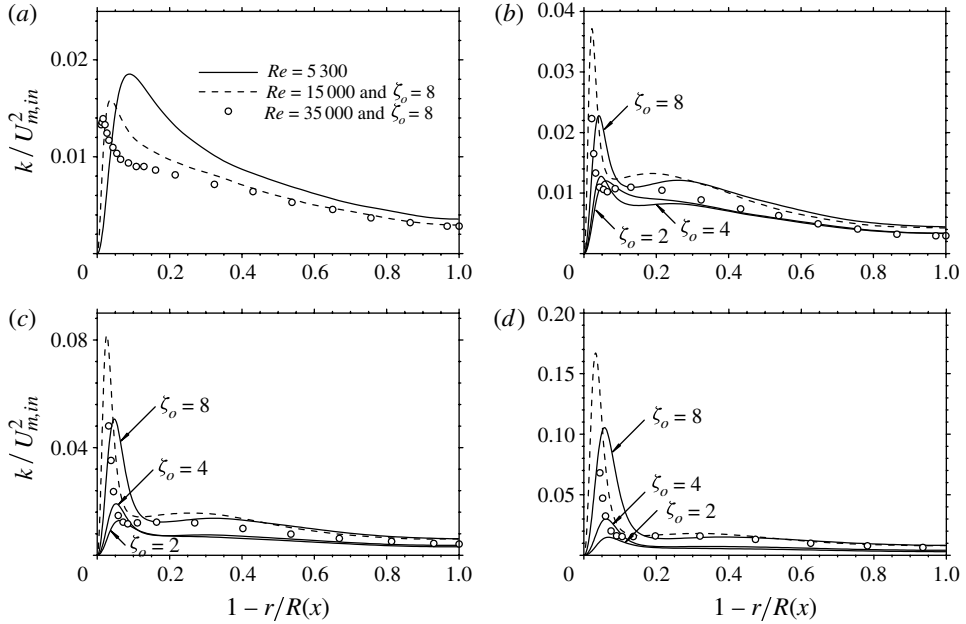
FIGURE 9. Turbulent kinetic energy $k = 0.5(u_x'^2 + u_r'^2 + u_\theta'^2)$ based on $U_{m,in}$. (*a*) Straight pipe; (*b*) $x/R = 3.34$; (*c*) $x/R = 4.90$; (*d*) $x/R = 6.66$. Circles show measurements at $Re = 35\,000$.
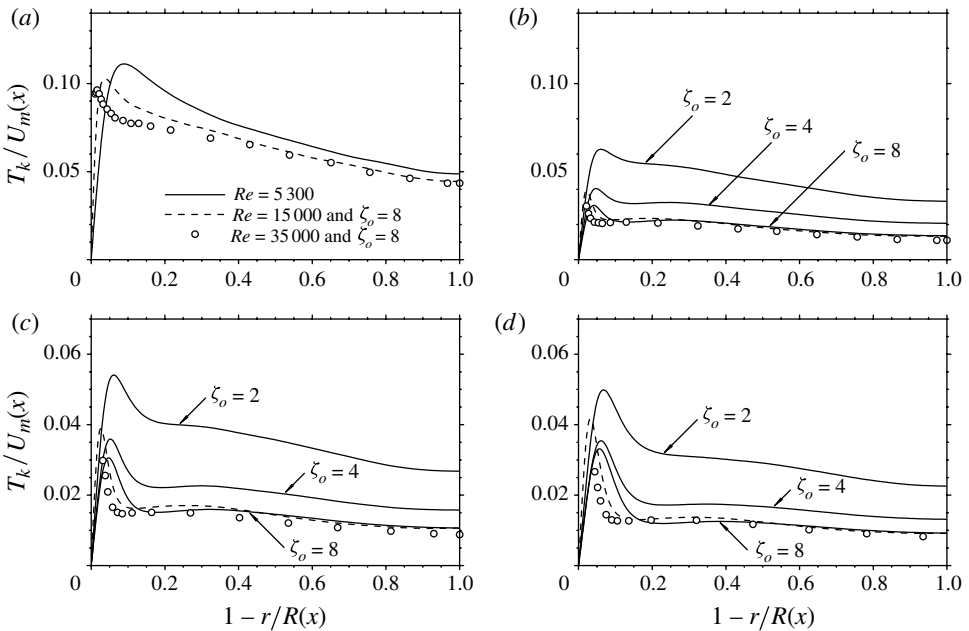

FIGURE 10. Local turbulence intensity $T_k = \{(u_x'^2 + u_r'^2 + u_\theta'^2)/3\}^{1/2}$ based on $U_m(x)$. (*a*) Straight pipe; (*b*) $x/R = 3.34$; (*c*) $x/R = 4.90$; (*d*) $x/R = 6.66$. Circles show measurements at $Re = 35\,000$.
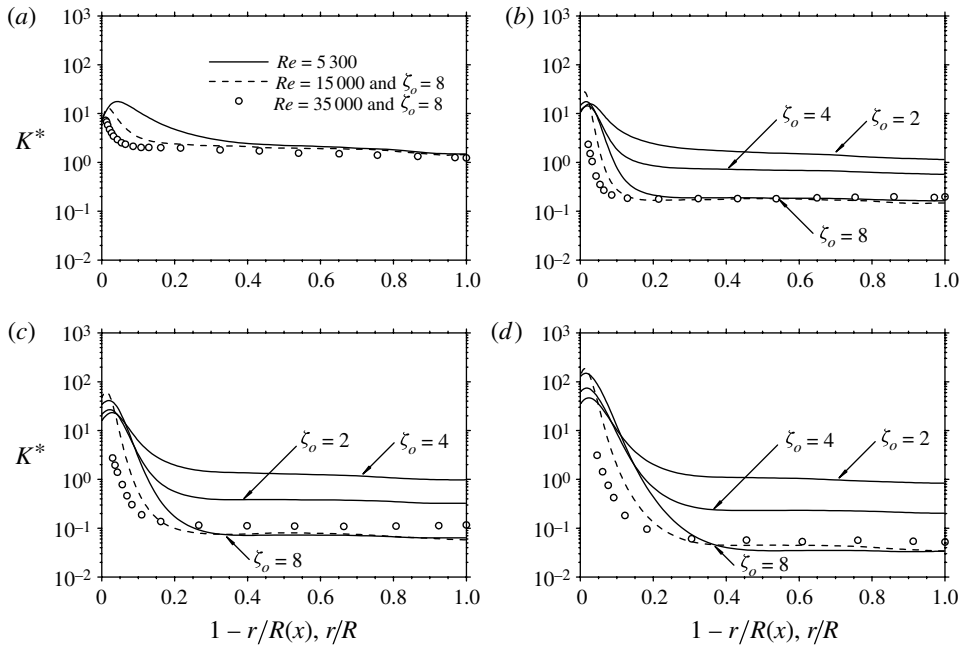
FIGURE 11. Energy partition parameter $K^* = 2u_x'^2/(u_r'^2 + u_\theta'^2)$. (*a*) Straight pipe; (*b*) $x/R = 3.34$; (*c*) $x/R = 4.90$; (*d*) $x/R = 6.66$.

shifted to the wall because of the contraction, as shown in figure 11. After $x/R = 4.90$, the peak value of K^* is significantly higher than that of the straight pipe due to the energy gain of the streamwise turbulent stress caused by the increase in the radial variation of the mean streamwise velocity near the wall. As the flow is accelerated, K^* gradually decreases in the outer region compared with that of the straight pipe. The decrease of K^* indicates that the energy is redistributed from the streamwise stress to the lateral stresses in the outer region by the contraction. For $\zeta_o = 8$, the region where the lateral turbulent stresses are very dominant ($K^* = 0.2$) for $Re = 15\,000$ is wider than that for $Re = 5300$, because of the increase of the uniform region of the mean streamwise velocity in the outer region as Re increases. The severe contraction greatly reduces the streamwise stress relative to the lateral stresses in the outer region.

For all of the flows, the Reynolds shear stress is practically unaffected by the contraction in the outer region as shown in figure 12, even though the turbulent stresses are affected by the severe contraction. For $\zeta_o = 8$, the Reynolds shear stress increases in the inner region, where the streamwise turbulent stress increases as the flow is accelerated. The negative value is observed in the near-wall region where the local minimum of the radial turbulence intensity is seen in the contraction. However, the small plateau near the wall in the distribution of the radial turbulence intensity (figure 7) and the negative region in the Reynolds shear stress disappear by the change of the coordinates from the cylindrical to the tangential and normal to the mean streamline.

To see the effects of the axisymmetric contraction, we consider the budget of Reynolds stress equations. The transport equation for the normal stresses by
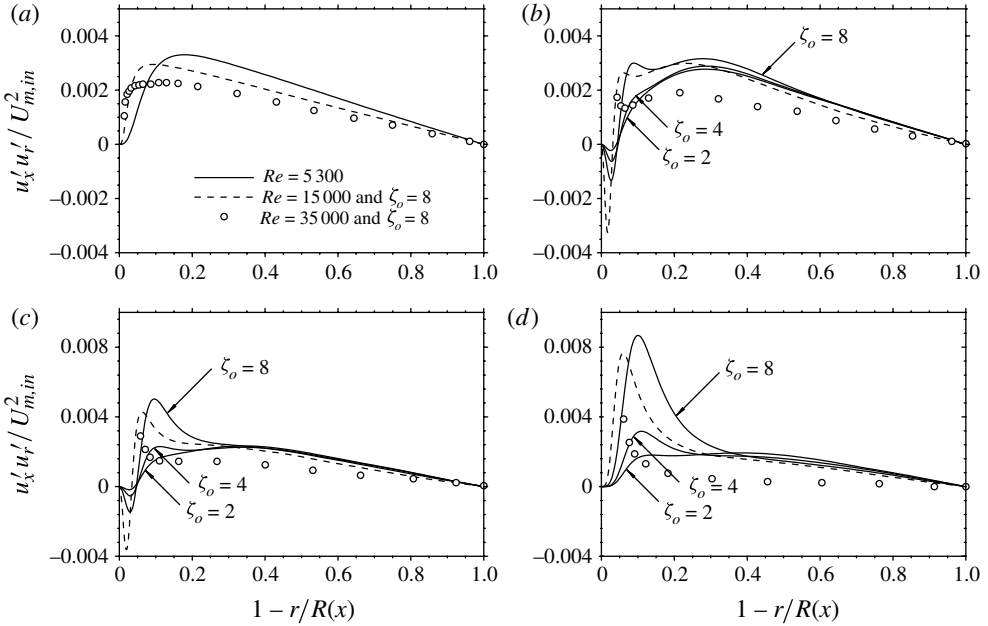
FIGURE 12. Reynolds shear stress based on $U_{m,in}$. (*a*) Straight pipe; (*b*) $x/R = 3.34$; (*c*) $x/R = 4.90$; (*d*) $x/R = 6.66$.

introducing the homogeneity in the azimuthal direction can be reduced as

$$
\left.
\begin{aligned}
0 = & \underbrace{-\frac{\partial \overline{u'_x u'_x}}{\partial t} - U_x \frac{\partial \overline{u'_x u'_x}}{\partial x} - U_r \frac{\partial \overline{u'_x u'_x}}{\partial r}}_{C_{xx}} \underbrace{-2\overline{u'_x u'_x}\frac{\partial U_x}{\partial x} - 2\overline{u'_x u'_r}\frac{\partial U_x}{\partial r}}_{P_{xx}} \\
& \underbrace{-2\overline{u'_x \frac{\partial p'}{\partial x}}}_{\Pi_{xx}} \underbrace{-\frac{2}{Re}\left[\overline{\left(\frac{\partial u'_x}{\partial x}\right)^2} + \overline{\left(\frac{\partial u'_x}{\partial r}\right)^2} + \overline{\left(\frac{1}{r}\frac{\partial u'_x}{\partial \theta}\right)^2}\right]}_{\varepsilon_{xx}} \\
& + T_{xx} + D_{xx}
\end{aligned}
\right\}, \quad (4.1)
$$

$$
\left.
\begin{aligned}
0 = & \underbrace{-\frac{\partial \overline{u'_r u'_r}}{\partial t} - U_x \frac{\partial \overline{u'_r u'_r}}{\partial x} - U_r \frac{\partial \overline{u'_r u'_r}}{\partial r}}_{C_{rr}} \underbrace{-2\overline{u'_x u'_r}\frac{\partial U_r}{\partial x} - 2\overline{u'_r u'_r}\frac{\partial U_r}{\partial r}}_{P_{rr}} \\
& \underbrace{-2\overline{u'_r \frac{\partial p'}{\partial r}}}_{\Pi_{rr}} \underbrace{-\frac{2}{Re}\left[\overline{\left(\frac{\partial u'_r}{\partial x}\right)^2} + \overline{\left(\frac{\partial u'_r}{\partial r}\right)^2} + \overline{\left(\frac{1}{r}\frac{\partial u'_r}{\partial \theta} - \frac{u'_\theta}{r}\right)^2}\right]}_{\varepsilon_{rr}} + T_{rr} + D_{rr}
\end{aligned}
\right\} \quad (4.2)
$$

$$
\left.
\begin{aligned}
0 = & \underbrace{-\frac{\partial \overline{u'_\theta u'_\theta}}{\partial t} - U_x \frac{\partial \overline{u'_\theta u'_\theta}}{\partial x} - U_r \frac{\partial \overline{u'_\theta u'_\theta}}{\partial r}}_{C_{\theta\theta}} \underbrace{-\frac{2}{r}\overline{u'_\theta u'_\theta}U_r}_{P_{\theta\theta}} \\
& \underbrace{-2\overline{u'_\theta \frac{1}{r}\frac{\partial p'}{\partial \theta}}}_{\Pi_{\theta\theta}} \underbrace{-\frac{2}{Re}\left[\overline{\left(\frac{\partial u'_\theta}{\partial x}\right)^2} + \overline{\left(\frac{\partial u'_\theta}{\partial r}\right)^2} + \overline{\left(\frac{1}{r}\frac{\partial u'_\theta}{\partial \theta} + \frac{u'_r}{r}\right)^2}\right]}_{\varepsilon_{\theta\theta}} \\
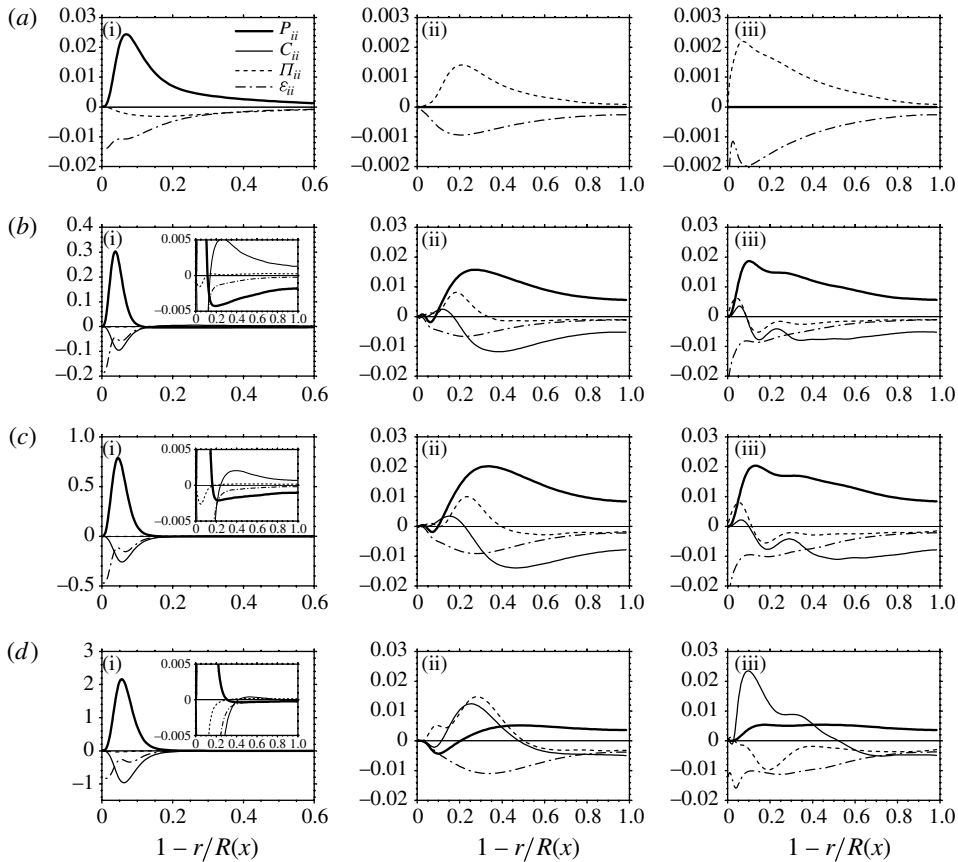& + T_{\theta\theta} + D_{\theta\theta}.
\end{aligned}
\right\} \quad (4.3)
$$

FIGURE 13. Budgets for normal stresses normalized by $U_{m,in}^3/R$ for $Re = 5300$ with $\zeta_o = 8$. (*a*) Straight pipe; (*b*) $x/R = 3.34$; (*c*) $x/R = 4.90$; (*d*) $x/R = 6.66$. (i) Streamwise stress; (ii) radial stress; (iii) azimuthal stress.

The terms on the right-hand side of the transport equations represent: C_{ii} = convection, P_{ii} = production, T_{ii} = turbulent transport, ε_{ii} = dissipation, D_{ii} = viscous diffusion and Π_{ii} = velocity pressure-gradient. Figure 13 shows the budgets for normal stresses normalized by $U_{m,in}^3/R$ for $Re = 5300$ with $\zeta_o = 8$. For the contraction, it is easy to see that the budget terms which are correlated to the mean velocity and the gradient of the mean velocity are more dominant than those which are correlated to the fluctuations in the outer region. As shown in figure 13(i), the production term of the streamwise stress has two different regions, like the streamwise stress itself in the contraction. P_{xx} increases with the increase of the local contraction ratio in the inner region, but becomes negative in the outer region. The first term of P_{xx} in (4.1) is always negative in the contraction due to the positive $\mathrm{d}U_x/\mathrm{d}x$. The second term of P_{xx} is strongly positive in the inner region, but becomes zero in the outer region. This is due to the rapid increase of U_x near the wall and the uniformity of U_x in the outer region, as shown in figure 6. For the contraction, the effect of this term is restricted within the inner region, whereas this term is always a dominant producing term for the straight pipe. However, in the inner region, the second term of P_{xx} increases as the flow is accelerated. In the outer region, P_{xx} is proportional to the streamwise stress due to

the same mean strain regardless of r, and thus the magnitude of P_{xx} decreases as the streamwise stress decreases. The convection term C_{xx} becomes the dominant producing term in the outer region.

The budgets of the radial stress are shown in figure 13(ii). For the straight pipe, the dissipation term ε_{rr} is the main sink term and the velocity pressure-gradient term Π_{rr} is the dominant source term. For the contraction, the production term P_{rr}, which is zero for the straight pipe, becomes the dominant producing term and the convection term C_{rr} becomes the dominant damping term in the outer region. The second term of P_{rr} in (4.2) is positive except near the wall region where U_r becomes a minimum (figure 6). This term is proportional to the radial stress itself in the outer region, because $\mathrm{d}U_r/\mathrm{d}r$ is constant as mentioned earlier. In the budget of the azimuthal stress shown in figure 13(iii), the velocity pressure-gradient term is dominant and is balanced by the dissipation term except very near the wall, where the viscous diffusion (not shown here) is very important for the straight pipe. For the contraction, $P_{\theta\theta}$ and $C_{\theta\theta}$ are the dominant producing and consuming terms in the outer region respectively, in the same way as P_{rr} and C_{rr} are for the radial budget. $P_{\theta\theta}$ has only one term in (4.3), which is always positive because of the negative radial velocity.

4.3. *Turbulent structure*

To assess the effects of the axisymmetric contraction on turbulent structure, we analysed the turbulent anisotropy. A convenient way to characterize the anisotropy is through the Reynolds stress anisotropy tensor as proposed by Lumley & Newman (1977), $b_{ij} = \tau_{ij}/\tau_{kk} - \delta_{ij}/3$, where τ_{ij} is the turbulent stress tensor and δ_{ij} is the Kronecker delta tensor. For isotropic turbulence, all elements of b_{ij} vanish. The diagonal elements of b_{ij} are restricted to $-1/3 < b_{ij} < 2/3$. The first invariant of b_{ij} is zero by definition, and the second and third invariants of b_{ij} are given by

$$I_2 = -b_{ij}b_{ji}/2 \quad \text{and} \quad I_3 = b_{ij}b_{jk}b_{ki}/3. \tag{4.4}$$

Lumley & Newman (1977) have shown that the cross-plots of the invariants $-I_2$ and I_3 for axisymmetric turbulence and for two-component turbulence define the anisotropy invariant map (AIM) that bounds all physically realizable turbulence. In the AIM, turbulence must exist within the area bounded by three lines; an upper straight line representing the state of two-component turbulence, and left and right boundaries originating from the bottom cusp, which correspond to two types of axisymmetric turbulence. The left and right boundaries correspond to 'disk-like' and 'rod-like' turbulence states (Lee & Reynolds 1985), respectively, and the bottom cusp characterizes isotropic turbulence. Figure 14 shows the AIM for $Re = 15\,000$ with $\zeta_o = 8$ in the outer region and in the near-wall region. As the flow enters the contraction, the turbulence quickly moves from a 'rod-like' to a 'disk-like' state in the outer region ($\zeta < 2$) due to the rapid decrease of the streamwise turbulent stress as shown in figure 8(*a*). As the flow develops, the turbulence moves along the left axisymmetric boundary towards a two-component axisymmetric turbulent 'disk' state due to the decrease in the streamwise stress and the linear increase of the lateral stresses. Along the centreline, the turbulence follows perfectly the left axisymmetric boundary, 'disk-like' state. This confirms that the lateral turbulent stresses are identical and increase whereas the streamwise stress decreases along the contraction at the centreline. In the near-wall region, the turbulence develops along the upper, two-component turbulence boundary, due to the increase of the streamwise stress in the inner region and the suppression of the radial stress by the wall. As the flow is accelerated, the streamwise stress becomes dominant and the turbulence moves
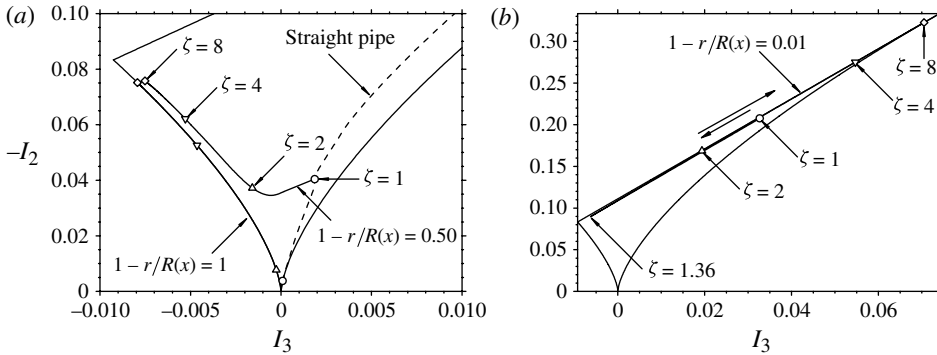
FIGURE 14. Anisotropy invariant map for $Re = 15\,000$ with $\zeta_o = 8$. (*a*) Outer region; (*b*) near-wall region.
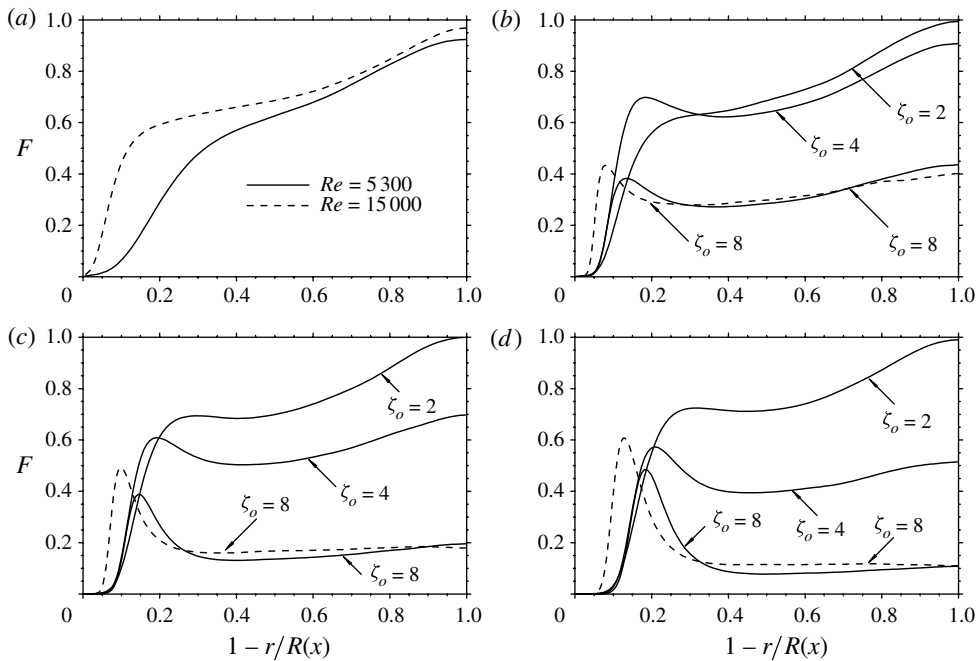

FIGURE 15. Anisotropy invariant function $F = 9I_2 + 27I_3 + 1$. (*a*) Straight pipe; (*b*) $x/R = 3.34$; (*c*) $x/R = 4.90$; (*d*) $x/R = 6.66$.

towards the one-component state of the upper right-hand corner. Another estimate of the overall anisotropy in the Reynolds stress tensor is given by the function $F = 9I_2 + 27I_3 + 1$, which is a measure of the approach towards either two-component turbulence ($F = 0$) or isotropic turbulence ($F = 1$). It is clear from the variation of F shown in figure 15 that the severe contraction pushes the turbulence towards two-component turbulence as the streamwise stress is being suppressed. For $\zeta_o = 2$, however, F remains mostly close to 1 and hence the turbulence state moves closer to an isotropic state due to the mild contraction ratio.
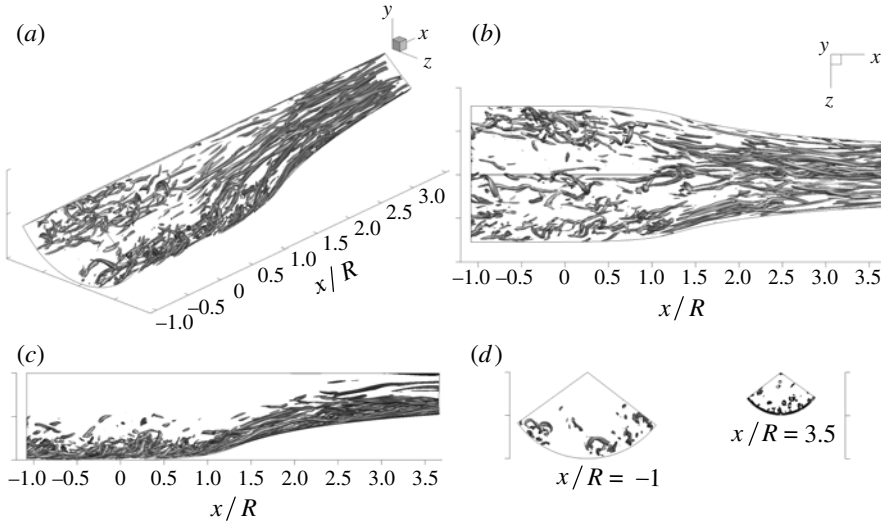
FIGURE 16. Vortical structures for $Re = 15\,000$ with $\zeta_o = 8$. (*a*) Perspective view; (*b*) top view; (*c*) side view; (*d*) rear and front views.

To observe the responses of the vortical structures to the contraction, we visualize the instantaneous vortical structures for $Re = 15\,000$ with $\zeta_o = 8$ using an iso-surface of the swirling strength λ_{ci} (figure 16), as proposed by Zhou *et al.* (1999). The swirling strength λ_{ci} is the imaginary part of the complex conjugate eigenvalue of the velocity gradient tensor. The swirling strength is a quantity that can be used to detect vortex cores and to distinguish vortical structures from shear regions. The iso-surface value of $\lambda_{ci}R/U_{m,in} = 4$ is used. The great difference between the straight pipe, $-1 < x/R < 0$, and the contraction, $x/R > 0$, is the presence of the spanwise vortical structure in the pipe. In the contraction, the axes of the spanwise vortical structures are stretched into the streamwise vortices. After $x/R > 1.5$, only the long streaky streamwise structures are observed. The streamwise vortical structures, including the aligned structures, are stretched in the mean flow direction in the initial region of the contraction, $0 < x/R < 1.5$, and the short stretched structures are merged in the flow direction and stretched significantly as the flow is accelerated. Some streaky structures are lifted to the centre region by the mean radial velocity.

The spatial characteristics of the streamwise velocity and vorticity fluctuations are obtained from the correlation coefficients $R_{u_x u_x}$ and $R_{\omega_x \omega_x}$, which are defined as

$$R_{u_x u_x}(\Delta x, r, \Delta\theta) = \frac{\langle u'_x(x_{ref}, r_{ref}, \theta)u'_x(x_{ref} + \Delta x, r, \theta + \Delta\theta)\rangle}{u'_{x,rms}(x_{ref}, r_{ref})u'_{x,rms}(x_{ref} + \Delta x, r)} \qquad (4.5)$$

and

$$R_{\omega_x \omega_x}(\Delta x, r, \Delta\theta) = \frac{\langle \omega'_x(x_{ref}, r_{ref}, \theta)\omega'_x(x_{ref} + \Delta x, r, \theta + \Delta\theta)\rangle}{\omega'_{x,rms}(x_{ref}, r_{ref})\omega'_{x,rms}(x_{ref} + \Delta x, r)}, \qquad (4.6)$$

where the angle bracket indicates an average over the azimuthal direction and time. Using the data of $Re = 15\,000$ with $\zeta_0 = 8$, the correlation coefficients are obtained and the radial reference location r_{ref} is $1 - r/R(x) = 0.5$ to observe the spatial characteristics in the outer region. Contours of the two-point autocorrelation coefficient
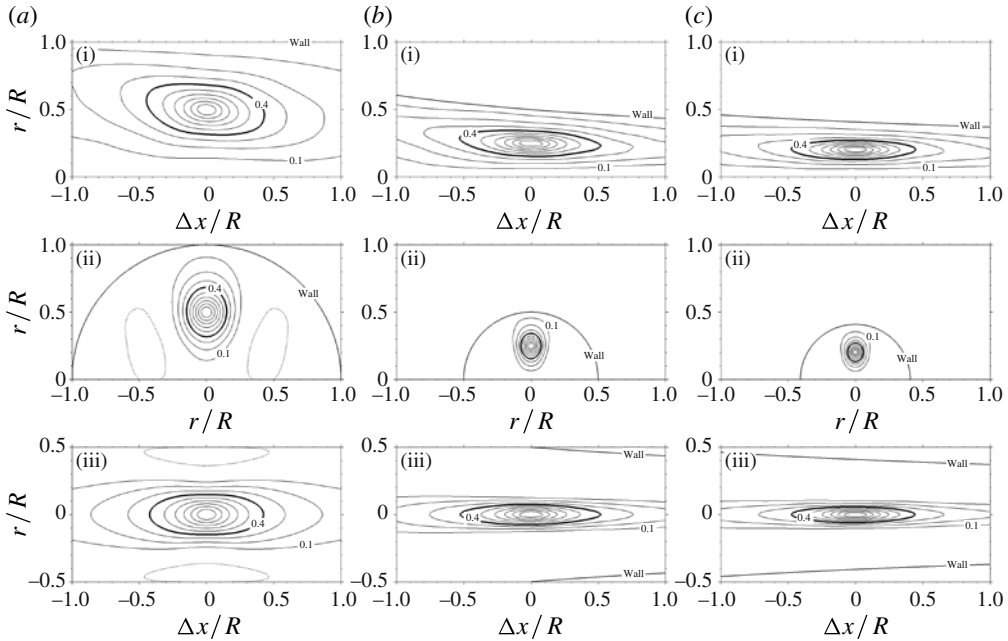
FIGURE 17. Contours of $R_{u_x u_x}(\Delta x, r, \Delta\theta)$ for $Re = 15\,000$ with $\zeta_o = 8$. (*a*) Straight pipe; (*b*) $x/R = 3.34$ ($\zeta = 4$); (*c*) $x/R = 4.90$ ($\zeta = 6$). (i) $\Delta\theta = 0$ in the x–r plane; (ii) $\Delta x = 0$ in the r–θ plane; (iii) top view of the x–θ plane at $1 - r/R(x) = 0.5$. The contour levels are from -0.9 to 0.9 in increments of 0.1. Negative contours are dashed and zero contours are not drawn.

of the streamwise velocity fluctuations are shown in figure 17. For reference, the correlation coefficients for the straight pipe are shown in figure 17(*a*). For the local contraction ratios $\zeta = 4$ and 6, the correlation coefficients are displayed in figures 17(*b*) and 17(*c*), respectively. Compared to the contours of the straight pipe, the contours of the contraction are shrunk along the radial and azimuthal directions, and are nearly unaffected along the streamwise direction. The ratio of the shrunk contours is the same as the contraction ratio of the local radius.

Contour plots of the two-point autocorrelation coefficient of the streamwise vorticity fluctuations are shown in figure 18. Compared to the contours of the straight pipe, the contours of the contraction are also shrunk along the radial and azimuthal directions. However, the contours in the contraction are more slender than those of $R_{u_x u_x}$. Along the streamwise direction, the contours are elongated with the same ratio as the increase in the local bulk velocity. The streamwise structure with positive correlation, which is inclined to the wall for the straight pipe, is aligned with the mean flow direction by the contraction. This is consistent with the behaviour of the instantaneous vortical structures as shown in figure 16.

It is reported that the vortical structures are closely related to the production of Reynolds shear stress (Robinson 1991). Moin, Adrian & Kim (1987) proposed that conditionally averaged vortical structures can be identified by carrying out a linear stochastic estimate (LSE) based on the velocity vector that makes the dominant contribution to the Reynolds shear stress. We examined the vortical structures associated with the production of Reynolds shear stress by using the method of Moin *et al.* (1987). The weighted joint probability density functions $u'_x u'_r$ p.d.f. (u'_x, u'_r) are
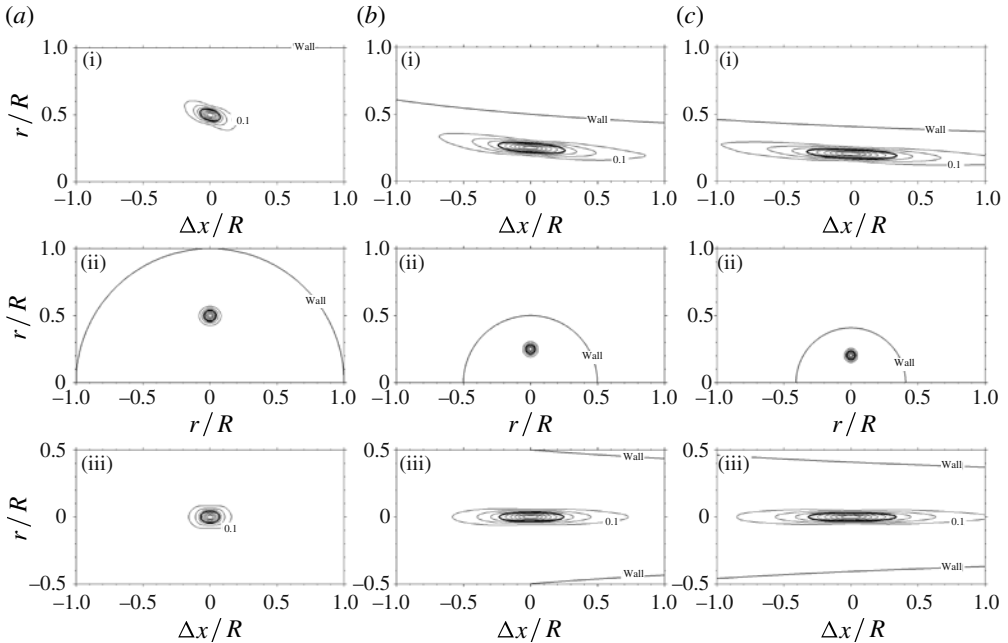
FIGURE 18. Contours of $R_{\omega_x \omega_x}(\Delta x, r, \Delta\theta)$ for $Re = 15\,000$ with $\zeta_o = 8$. (*a*) Straight pipe; (*b*) $x/R = 3.34$ ($\zeta = 4$); (*c*) $x/R = 4.90$ ($\zeta = 6$). (i) $\Delta\theta = 0$ in the *x*–*r* plane; (ii) $\Delta x = 0$ in the *r*–θ plane; (iii) top view of the *x*–θ plane at $1 - r/R(x) = 0.5$. The contour levels are from -0.9 to 0.9 in increments of 0.1. Negative contours are dashed and zero contours are not drawn.
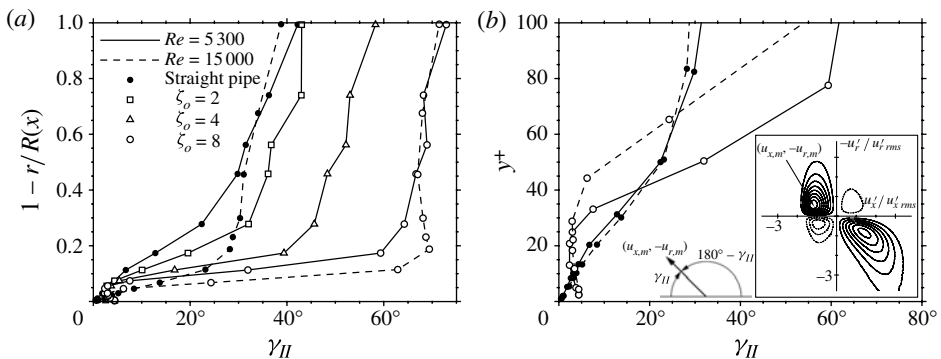

FIGURE 19. Angle of velocity vector with the maximum contribution to local Reynolds shear stress at $x/R = 3.34$ as a function of (*a*) $1 - r/R(x)$ and (*b*) y^+. The inset shows an example of contours of probability weighted Reynolds shear stress $u_x' u_r'$ p.d.f. (u_x', u_r') at $y^+ = 5.4$ for the straight pipe with $Re = 15\,000$.

examined to determine the conditional event vector $u_E = (u_{x,m}, -u_{r,m})$. These events are detected by finding the maximum values of $u_x' u_r'$ p.d.f. (u_x', u_r') in the second quadrant Q2. An example contour plot of the probability weighted Reynolds shear stress is shown in the inset of figure 19. The event angles $\gamma_{II} = \tan^{-1}(-u_{r,m}/u_{x,m})$ defined by u_E, which maximizes the contribution to the Reynolds shear stress
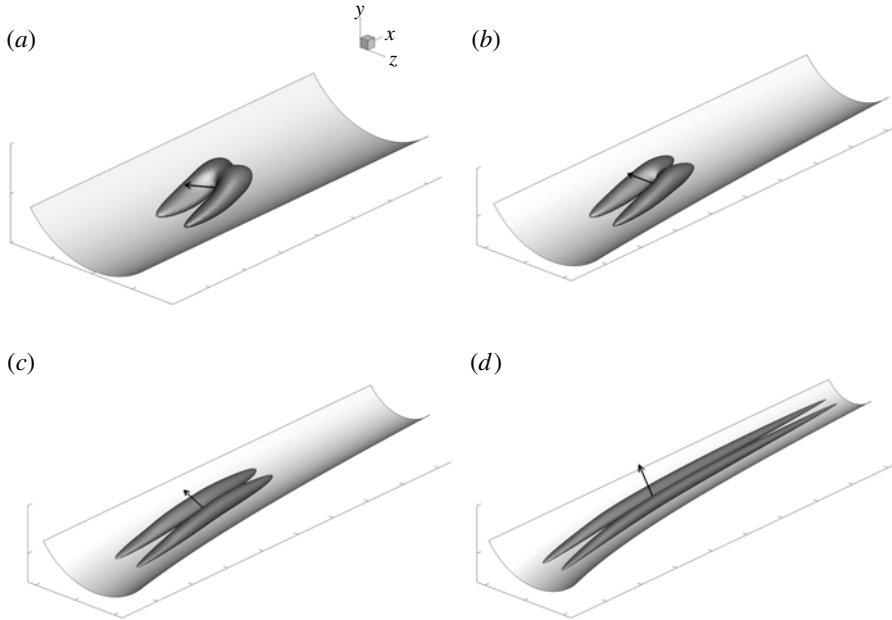
FIGURE 20. Vortical structures of the linearly estimated flow field with the Q2 event vector $u_E = (u_{x,m}, -u_{r,m})$ at $x/R = 3.34$ and $1 - r/R(x) = 0.28$ ($y^+ = 50$ for the straight pipe) for $Re = 5300$. (*a*) Straight pipe; (*b*) $\zeta_o = 2$; (*c*) $\zeta_o = 4$; (*d*) $\zeta_o = 8$. The vortices are identified with an iso-surface of swirling strength (30 % of maximum λ_{ci}). The vectors represent the velocity events used in the estimation. The distance between ticks on each axis is $0.5R$.

at $x/R = 3.34$, are represented in figure 19. It is easy to see that the effects of *Re* are relatively small for the same geometry in the outer region as shown in figure 19(*a*). As a function of y^+, the profile for the straight pipe of $Re = 5300$ is in good agreement with that of $Re = 15\,000$ at $y^+ < 100$; however, the profiles for the contraction of $Re = 5300$ and $15\,000$ are different. As ζ_o increases, the event angles increase in the outer region. This is consistent with the observation that the radial turbulent stress increases in the outer region with the increase in ζ_o, whereas the Reynolds shear stress remains fairly unaffected by the contraction.

Conditional vortical structures around the Q2 events that make the dominant contribution to the mean Reynolds shear stress at $x/R = 3.34$ and $1 - r/R(x) = 0.28$ ($y^+ = 50$ for the straight pipe) for $Re = 5300$ are compared in figure 20. We introduce LSE because direct computation of the conditional averages is impractical. It is well known that LSE is a robust conditionally averaged approximation that provides satisfactory results for various turbulent fields (Adrian *et al.* 1989). The linear estimate of the conditional average is given by

$$\langle u_i(x + r) | u_{x,m}(x), -u_{r,m}(x) \rangle = L_{i1} u_{x,m}(x) - L_{i2} u_{r,m}(x), \tag{4.7}$$

with $i = x$, r and θ and

$$\begin{bmatrix} L_{i1} \\ L_{i2} \end{bmatrix} = \frac{1}{\langle u_x'^2 \rangle \langle u_r'^2 \rangle - \langle u_x' u_r' \rangle^2} \begin{bmatrix} \langle u_r'^2 \rangle & -\langle u_x' u_r' \rangle \\ -\langle u_x' u_r' \rangle & \langle u_x'^2 \rangle \end{bmatrix} \begin{bmatrix} \langle u_x'(x) u_i'(x + r) \rangle \\ \langle u_r'(x) u_i'(x + r) \rangle \end{bmatrix}. \tag{4.8}$$

The conditional structures are identified with an iso-surface of λ_{ci} based on the conditionally averaged velocity fluctuations. As ζ_o increases, the conditional structure
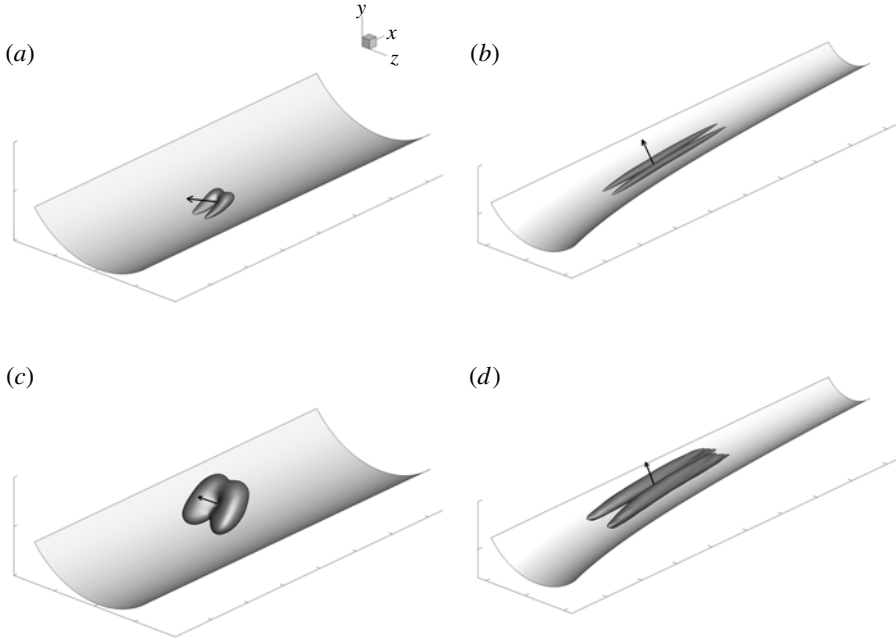
FIGURE 21. Vortical structures of the linearly estimated flow field with the Q2 event vector $u_E = (u_{x,m}, -u_{r,m})$ at $x/R = 3.34$ for $Re = 15\,000$. (a, b) $1 - r/R(x) = 0.11$ ($y^+ = 50$ for the straight pipe); (c, d) $1 - r/R(x) = 0.46$ ($y^+ = 203$ for the straight pipe). The vortices are identified with an iso-surface of swirling strength (30 % of maximum λ_{ci}). The vectors represent the velocity events used in the estimation. The distance between ticks on each axis is $0.5R$.

changes from hairpin vortices (figures 20a and 20b) to counter-rotating pairs of streamwise vortices (figures 20c and 20d). The streamwise length scale of the conditional structure is significantly elongated in the mean flow direction as ζ_o increases. The conditional structure, which is inclined to the wall for the straight pipe, is aligned with the mean flow direction by the contraction. To see the difference between the inner and outer regions, the conditional vortical structures associated with the Q2 event at $1 - r/R(x) = 0.11$ and 0.46 for $Re = 15\,000$ are shown in figure 21. These locations are at $y^+ = 50$ and 203 correspondingly for the straight pipe. It is apparent that the developments of the conditional structures in the inner and outer regions are similar. The hairpin vortices are changed into counter-rotating pairs of streamwise vortices in both the inner and outer regions. The vortical structures are stretched with the same streamwise length scale in both regions detected by the iso-surface of the swirling strength (30 % of maximum λ_{ci}), while the vortical structure in the outer region is larger than that in the inner region for the straight pipe. However, the maximum value of λ_{ci} for the inner structure is larger than that for the outer one in the contraction. This indicates that the individual vortices located in the inner region are more stretched than those in the outer region.

5. Summary and conclusions

Detailed experimental and numerical studies have been performed to elucidate the effects of an axisymmetric contraction fitted to a fully developed turbulent pipe flow.

Direct numerical simulations were carried out at $Re = 5300$ and $15\,000$ and experiment was performed at $Re = 35\,000$ with the same geometry where the contraction ratio is $\zeta_o = 8$. The effects of the contraction ratio were examined by using DNS with three contraction ratios, $\zeta_o = 2$, 4 and 8. This study verified earlier findings that the turbulence structure is significantly modified by the contraction. The turbulent kinetic energy decays rapidly in the core region of the contraction when scaled with the local bulk velocity. Very quickly the turbulence tends towards two-component turbulence where the streamwise component virtually disappears. We found that the shear stress distribution is little affected by the contraction. However, the radial variation of the streamwise turbulent energy has two different regions in the contraction. In the near-wall region the dominant turbulent energy producing velocity gradient $\partial U_x / \partial r$ grows rapidly along the contraction, leading to a significant increase in near-wall energy. As Re increases, the near-wall peak value increases. Since the contraction causes the flow in the core region to become more homogeneous, the production from $\partial U_x / \partial r$ disappears over the bulk part of the cross-section and is replaced by the negative turbulent production, primarily from the streamwise acceleration $-u_x'^2 \partial U_x / \partial x$. In the outer region, the dominant producing term is the convection term, not the pressure-strain term, which redistributes turbulent energy from the lateral stresses. At the same time, the two lateral stresses receive energy from the two positive production terms $-u_r'^2 \partial U_r / \partial r$ and $-u_\theta'^2 U_r / r$, which do not contribute in a fully developed pipe flow. The turbulence intensities for $\zeta_o = 8$ in the outer region are almost the same despite the differences in Re, and thus the contraction ratio is the main parameter for characterizing the second-order turbulence statistics. An invariant analysis confirmed that most of the flow in the contraction is in a state close to two-component turbulence. This is because the streamwise stress in the core region is significantly suppressed, while the wall-normal stress is suppressed near the wall. An intermediate region exists between these two regions, where the flow tends towards isotropy for the Reynolds stress tensor as the contraction ratio increases. The acceleration causes a stretching of the turbulent vortical structures in such a way that hairpin-type vortices found in the pipe are stretched into two parallel, counter-rotating vortices in the contraction. This is so strong that the spanwise braid in the original structure is broken. The vortical structure, which is inclined with respect to the wall for the straight pipe, is now aligned with the mean flow direction, and the stretching effect appears to be virtually independent of the radial position.

Appendix

The boundary layer equations for an axisymmetric contraction pipe flow in the body-fitted (s, n) coordinate system are

$$\frac{\partial}{\partial s}[U_s r] + \frac{\partial}{\partial n}[U_n h r] = 0, \tag{A 1}$$

$$\frac{U_s}{h}\frac{\partial U_s}{\partial s} + U_n \frac{\partial U_s}{\partial n} + \frac{\kappa\, U_s U_n}{h} = -\frac{1}{h\rho}\frac{\partial P}{\partial s} + \frac{1}{r}\frac{\partial}{\partial n}\frac{r}{h}\left[\nu\frac{\partial}{\partial n}(hU_s)\right]$$
$$+ \frac{1}{r}\frac{\partial}{\partial n}\left[r\frac{\tau_{sn}}{\rho}\right] + \frac{2\kappa}{h}\frac{\tau_{sn}}{\rho}, \tag{A 2}$$
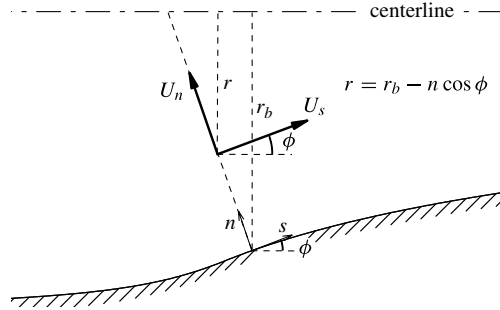
FIGURE 22. Schematic diagram of the coordinate system.

$$\frac{1}{\rho}\frac{\partial P}{\partial n} = \frac{\kappa}{h}U_s^2, \tag{A 3}$$

where the local radius is $r = r_b - n\cos\varphi$, r_b is the radius of the body, $1/r_b$ is the transverse curvature, κ is the longitudinal curvature with the definition of $h = 1 + \kappa n$, and ϕ is the inclination angle. A schematic configuration of the coordinate system is shown in figure 22. The boundary conditions are $n = U_s(s, 0) = U_n(s, 0) = \tau_{sn}(s, 0) = 0$.

The appropriate outer variables for similarity analysis are

$$U_s = \frac{U_c}{h}\frac{\partial f(\eta, s)}{\partial \eta}, \quad \tau = \rho U_c^2 T(\eta, s), \quad \eta = \int \frac{r}{\delta h}\,\mathrm{d}n. \tag{A 4}$$

Next, let $U_c(s) = U_{s,\delta}s^m$ and $m = (\delta/U_c)(\mathrm{d}U_c/\mathrm{d}\delta)$; the inner variables are

$$\frac{U_s}{u_\tau} = U_s^+(n^+, s), \quad \frac{\tau_{sn}}{\rho u_\tau^2} = \tau_{sn}^+(n^+, s), \quad \frac{nu_\tau}{\nu} = n^+. \tag{A 5}$$

The addition of δ and ν to the radius $r_b = a$ leads to three non-dimensional parameters δ/a, $a^+ = au_\tau/\nu$ and $\delta^+ = \delta u_\tau/\nu$. Considering the effect of longitudinal and transverse curvatures, the law of the wall and the defect law are expressed as (Afzal & Narasimha 1976)

$$\text{law of the wall: } U_s^+(n^+) = A\ln n^+ + B\left(\frac{au_\tau}{\nu}, \frac{u_\tau}{\kappa\nu}\right), \tag{A 6}$$

$$\text{defect law: } \frac{U_{s,\delta} - U_s}{u_\tau} = -A\ln\frac{n}{\delta} + D\left(\frac{\delta}{a}, \kappa\delta\right). \tag{A 7}$$

Figure 23 shows the law of the wall and the defect law and figure 24 shows the Reynolds stresses. Under the strong favourable pressure gradient, the Reynolds stresses are weakened (Cal & Castillo 2008). This reduction in energy applies in the core region for all the stresses. However, the near-wall behaviour is quite complicated, and different for the various stresses. While the u_n' and u_θ' components decrease continuously along the contraction all across the radius, u_s' first decreases rapidly near the surface, but then increases with distance. This is due to the strong energy production caused by the rapid increase in the mean velocity gradient near the wall as the flow accelerates through the contraction. Due to this complex stress development, where some increase and some decrease in the same flow domain, it appears impossible to find similarity solutions for the turbulent stresses. As the stresses
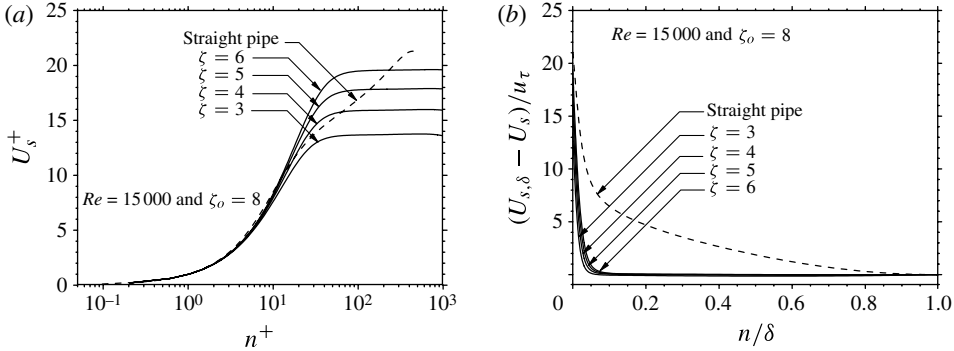
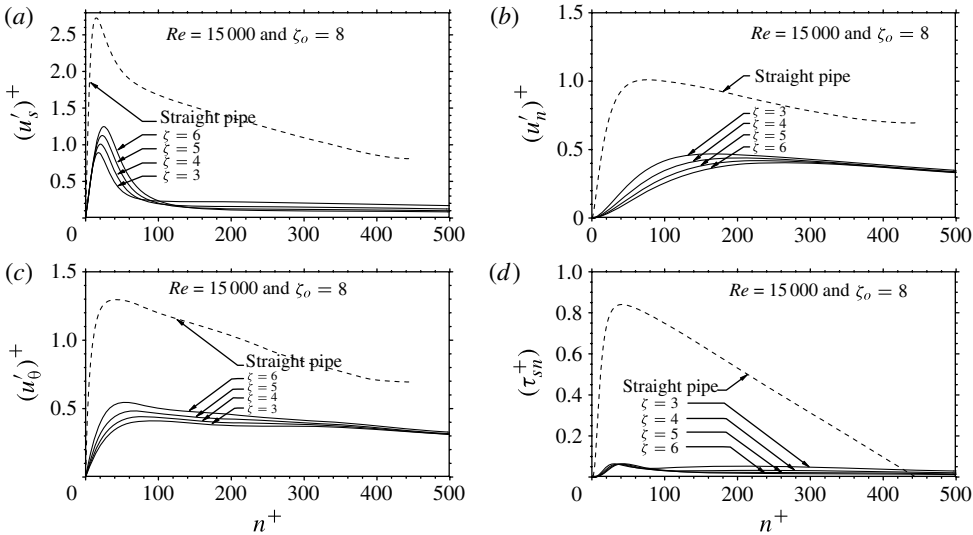FIGURE 23. (*a*) Law of the wall and (*b*) velocity defect law.

FIGURE 24. Profiles of (*a*) u'_s, (*b*) u'_n, (*c*) u'_θ and (*d*) τ_{sn}.

decrease, (A 1)–(A 3) in the outer variables become (Davis, Whitehead & Wornom 1971)

$$f''' + \frac{1}{R_t^2}(\alpha f + 2A - 2B)f'' + \frac{\beta}{R_t^2}(1 - f'^2) - \frac{2\beta h^2}{R_t^2}\int_\eta^\infty \frac{\kappa}{h}(1 - f'^2)\,d\eta = 0 \quad (A 8)$$

where $R_t = r/r_b$, $\alpha = g\,(U_c g)'\,/r_b^2$, $\beta = U'_c g^2/r_b^2$, $A = g\cos\phi/r_b^2$ and $B = g\kappa/r_b$. When the transverse and longitudinal curvatures become very small $1/r_b \to 0$ and $\kappa \to 0$, assuming $A = B = \phi = \alpha - 1 = 0$, (A 8) returns to the Falkner–Skan equation,

$$f''' + ff'' + \beta(1 - f'^2) = 0. \quad (A 9)$$

In terms of the outer variable $F(\eta) = 1 - f'(\eta)$, the Falkner–Skan equation is expressed as (Cal & Castillo 2008)

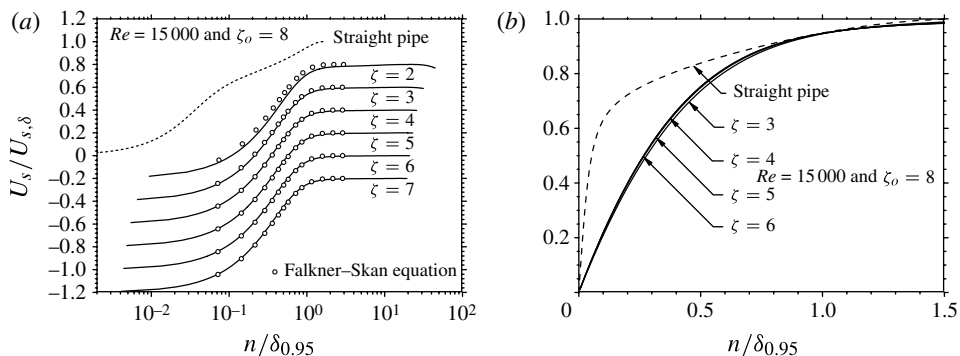$$cF'' + \eta F' - F' \int_0^\eta F\,d\eta + \beta(2F - F'^2) = 0. \quad (A 10)$$

FIGURE 25. (*a*) Falkner–Skan equation (*b*) velocity profiles.

Comparison of the present data with the Falkner–Skan equation in figure 25(*a*) guarantees the above assumption. Finally, the velocity profiles indicate a self-similarity in figure 25(*b*).

REFERENCES

ADRIAN, R. J., JONES, B. G., CHUNG, M. K., HASSAN, Y., NITHIANANDAN, C. K. & TUNG, A. T. C. 1989 Approximation of turbulent conditional averages by stochastic estimation. *Phys. Fluids* A **1**, 992–998.

AFZAL, N. & NARASIMHA, R. 1976 Axisymmetric turbulent boundary layer along a circular cylinder at constant pressure. *J. Fluid Mech.* **74**, 113–128.

AKSELVOLL, K. & MOIN, P. 1995. Report no. TF-63, Thermosciences Division, Department of Mechanical Engineering, Stanford University.

BAKKEN, O. M. & KROGSTAD, P.-Å 2004 A velocity dependent effective angle method for calibration of X-probes at low velocities. *Exp. Fluids* **37**, 146–152.

BATCHELOR, G. K. 1953 *The Theory of Homogeneous Turbulence*. Cambridge University Press.

CAL, R. B. & CASTILLO, L. 2008 Similarity analysis of favourable pressure gradient turbulent boundary layers with eventual quasilaminarization. *Phys. Fluids* **20**, 105106.

CHOI, H., MOIN, P. & KIM, J. 1993 Direct numerical simulation of turbulent flow over riblets. *J. Fluid Mech.* **255**, 503–539.

COMTE-BELLOT, G. & CORRSIN, S. 1966 The use of a contraction to improve the isotropy of grid-generated turbulence. *J. Fluid Mech.* **25**, 657–682.

DAVIS, R. T., WHITEHEAD, R. E. & WORNOM, S. F. 1971 The development of an incompressible boundary-layer theory valid to second order. *Heat Mass Transfer.* **4**, 167–177.

DURST, F., JOVANOVIĆ, J. & SENDER, J. 1995 LDA measurements in the near-wall region of a turbulent pipe flow. *J. Fluid Mech.* **295**, 305–335.

ERTUNÇ, Ö. & DURST, F. 2008 On the high contraction ratio anomaly of axisymmetric contraction of grid-generated turbulence. *Phys. Fluids* **20**, 025103.

HUSSAIN, A. K. M. F. & RAMJEE, V. 1976 Effects of the axisymmetric contraction shape on incompressible turbulent flow. *Trans. ASME: J. Fluids Engng* **98**, 58–69.

KIM, K., BAEK, S. J. & SUNG, H. J. 2002 An implicit velocity decoupling procedure for the incompressible Navier–Stokes equations. *Intl J. Numer. Meth. Fluids* **38**, 125–138.

LEE, M. & REYNOLDS, W. 1985 Numerical experiments on the structure of homogeneous turbulence. *Rep.* TF-24, Thermoscience Division, Stanford University.

LUMLEY, J. L. & NEWMAN, G. R. 1977 The return to isotropy of homogeneous turbulence. *J. Fluid Mech.* **82**, 161–178.

MOIN, P., ADRIAN, R. J. & KIM, J. 1987 Stochastic estimation of organized structures in turbulent channel flow. In *Sixth Symposium on Turbulent Shear Flows*, Toulouse, France, pp. 16.9.1–16.9.8.

NAWRATH, S. J., KHAN, M. M. K. & WELSH, M. C. 2006 An experimental study of scale growth rate and flow velocity of a super-saturated caustic–aluminate solution. *Intl J. Miner. Process.* **80**, 116–215.

POPE, S. B. 2000 *Turbulent Flows.* Cambridge University Press.

PRANDTL, L. 1933 Attaining a steady air stream in wind tunnels. *NACA Tech. Mem.* 726.

ROBINSON, S. K. 1991 Coherent motions in the turbulent boundary layer. *Annu. Rev. Fluid Mech.* **23**, 601–639.

SAVILL, A. M. 1987 Recent developments in rapid-distortion theory. *Annu. Rev. Fluid Mech.* **19**, 531–575.

SPEKREIJSE, S. P. 1995 Elliptic grid generation based on Laplace equations and algebraic transformation. *J. Comput. Phys* **118**, 38–61.

SREENIVASAN, K. R. & NARASIMHA, R. 1978 Rapid distortion of axisymmetric turbulence. *J. Fluid Mech.* **84**, 497–516.

TAYLOR, G. I. 1935 Turbulence in a contracting stream. *Z. Angew. Math. Mech.* **15**, 91–96.

DEN TOONDER, J. M. J. & NIEUWSTADT, F. T. M. 1997 Reynolds number effects in a turbulent pipe flow for low to moderate Re. *Phys. Fluids* **9**, 3398–3409.

UBEROI, M. S. 1956 Effect of wind-tunnel contraction on free stream turbulence. *J. Aero. Sci.* **23**, 754–764.

UBEROI, M. S. & WALLIS, S. 1966 Small axisymmetric contraction of grid turbulence. *J. Fluid Mech.* **24**, 539–543.

WU, X. & MOIN, P. 2008 A direct numerical simulation study on the mean velocity characteristics in turbulent pipe flow. *J. Fluid Mech.* **608**, 81–112.

ZHOU, J., ADRIAN, R. J., BALACHANDAR, S. & KENDALL, T. M. 1999 Mechanisms for generating coherent packets of hairpin vortices in channel flow. *J. Fluid Mech.* **387**, 353–396.